J. Fluid Mech. (1985), *vol.* 161, *pp.* 371–403
Printed in Great Britain

The effect of concave surface curvature on turbulent boundary layers

By P. H. HOFFMANN†, K. C. MUCK‡ AND P. BRADSHAW
Department of Aeronautics, Imperial College, London

(Received 24 April 1984 and in revised form 8 July 1985)

The response of a turbulent boundary layer to suddenly applied concave surface curvature with $\delta/R = 0.01$–0.02 is investigated. The main conclusion of this and the companion paper by Muck, Hoffmann & Bradshaw (1985) is that the effects of concave (destabilizing) and convex (stabilizing) curvature on boundary layers – and presumably on other shear layers – are totally different, even qualitatively. As shown in Muck, Hoffmann & Bradshaw (1985), convex curvature tends to attenuate the pre-existing turbulence and, at least in the case of mild curvature, there are no large changes in statistical average eddy shape. Concave curvature, on the other hand, can lead to the quasi-inviscid generation of longitudinal ('Taylor–Görtler') vortices, and we show that significant changes in the turbulence structure are induced both directly by the curvature and indirectly by the vortices.

1. Introduction

This paper is one of a series on complex turbulent flows, defined as shear layers distorted by an extra rate of strain or interacting with another turbulence field. Quasi-steady longitudinal vortices have been found in turbulent boundary layers on concave surfaces by many workers, beginning with Tani (1962). They are generated by the same, essentially inviscid, mechanism as in Rayleigh–Taylor–Görtler instability of laminar shear layers whose angular momentum decreases radially outward. Just as vortices can amplify in curved laminar flows despite the presence of some viscous diffusion, they can also grow in the presence of turbulent diffusion. In turbulent flow the vortices are bound to wander from side to side because of turbulence in the shear layer or the larger-scale turbulence or unsteadiness in the free stream. However, even mean-flow measurements can show clear spanwise variations, indicating that the vortices wander about preferred lateral positions: these are found to be determined by steady non-uniformities in the oncoming flow, notably those shed from the damping screens of a wind or water tunnel. The spanwise wavelength is usually about twice the boundary-layer thickness, but the spacing and amplitude are influenced by the initial disturbances. The wavelength of spanwise variations induced in flat-surface boundary layers by damping screens (which produce a wide range of disturbance wavelengths) increases downstream, roughly proportionally to the boundary-layer thickness. However, there seem to be no curved-flow measurements over a large enough streamwise distance to show conclusively that the number of vortices decreases as the boundary layer grows, except for an apparent decrease in vortex strength near the downstream end of the rig used by So & Mellor (1975).

† Present address: Dept of Civil and Aero. Engng, Royal Melbourne Institute of Technology, Melbourne, Vic. 3000, Australia.

‡ Present address: Research Divn., United Technologies – Carrier Corp., Syracuse, NY 13221, USA.

Jeans & Johnston (1982) found large-scale 'sweeps' and 'ejections' that did not have preferred spanwise locations and did not give rise to well-defined vortices. They used a water tunnel with very thin damping-screen wires (Reynolds number based on wire diameter less than 10): also, the measured turbulence level in their test section was rather high (1.3% including instrument 'noise'). Either may have led to an unusually large ratio of unsteadiness to fixed disturbance and thus to the apparent absence of longitudinal vortices. Ramaprian & Shivaprasad (1978) found no trace of vortices in time-averaged measurements, but they attributed this to inadequate test-section width rather than lateral wandering. Hunt & Joubert (1979), on the other hand, attributed the presence of quasi-steady vortices in their curved-duct flow to the constraint of the sidewalls: one would expect the effect of upstream disturbances to have died out, by definition, in fully developed duct flow. Johnston, Halleen & Lezius (1972) found that, in a rotating duct flow, transient vortices appeared at a curvature parameter equivalent to about $\delta/R = 0.01$, and became more nearly steady at $\delta/R = 0.02$: both values are well above the prediction of laminar-instability theory adapted by replacing the molecular viscosity with an estimated eddy viscosity (e.g. So & Mellor 1975).

In the present work, with δ/R initially about 0.01, a naturally occurring vortex pattern was found, but small artificial disturbances were introduced into the boundary layer to trigger a steadier and more regular vortex pattern. So as to produce vortices in the working section while minimizing other kinds of flow disturbance, the generators were located in the settling chamber of the wind tunnel. For the main tests we chose the smallest generators that imposed a satisfactorily regular skin-friction pattern, and the spacing that produced the largest amplification of spanwise variations down the length of the curved region. This technique is in the same spirit as the well-accepted use of controlled disturbances in transition experiments: in both cases, real-life flows contain a spectrum of disturbances, but the flow response is best investigated by choosing one representative disturbance wavenumber at a time. Our measurements agree with the usual finding that the amplified range of spanwise wavelengths is rather small and centred about a wavelength of approximately twice the boundary-layer thickness. The same technique has been used by Barlow & Johnston (1985), whose vortex generators were mounted in the working section and produced much larger disturbances than ours. An analogous method of excitation was used by Moser & Moin (1984) in a direct numerical simulation (complete time-dependent Navier–Stokes solution; not a large-eddy simulation alone) of curved-channel flow. They imposed periodic boundary conditions such that the instantaneous downstream outflow was fed back as the upstream inflow. This generated longitudinal vortices of wavelength necessarily the width of the computational domain, about twice the shear-layer thickness. In both the simulation and those experiments where a vortex pattern is observed, dimensionless structure parameters of the turbulence show strong spanwise periodicity, implying that structural changes are imposed by the vortex pattern as well as directly by the curvature. The structural changes bear some resemblance to those found in artificially generated vortex pairs on flat surfaces by Shibl & Bradshaw (1985) and Mehta & Bradshaw (1985) but the resemblance is not close enough to be quantitatively useful.

The present paper, like Muck, Hoffmann & Bradshaw (1985, hereinafter referred to as I), is a continuation of the work of Meroney & Bradshaw (1975), using the same test rig in which a well-developed low-speed turbulent boundary layer encounters a longitudinally curved surface with a radius of curvature about 100 times the initial thickness of the boundary layer. A general introduction to the work and the previous literature is given in I, where it is pointed out that the effects of concave and convex

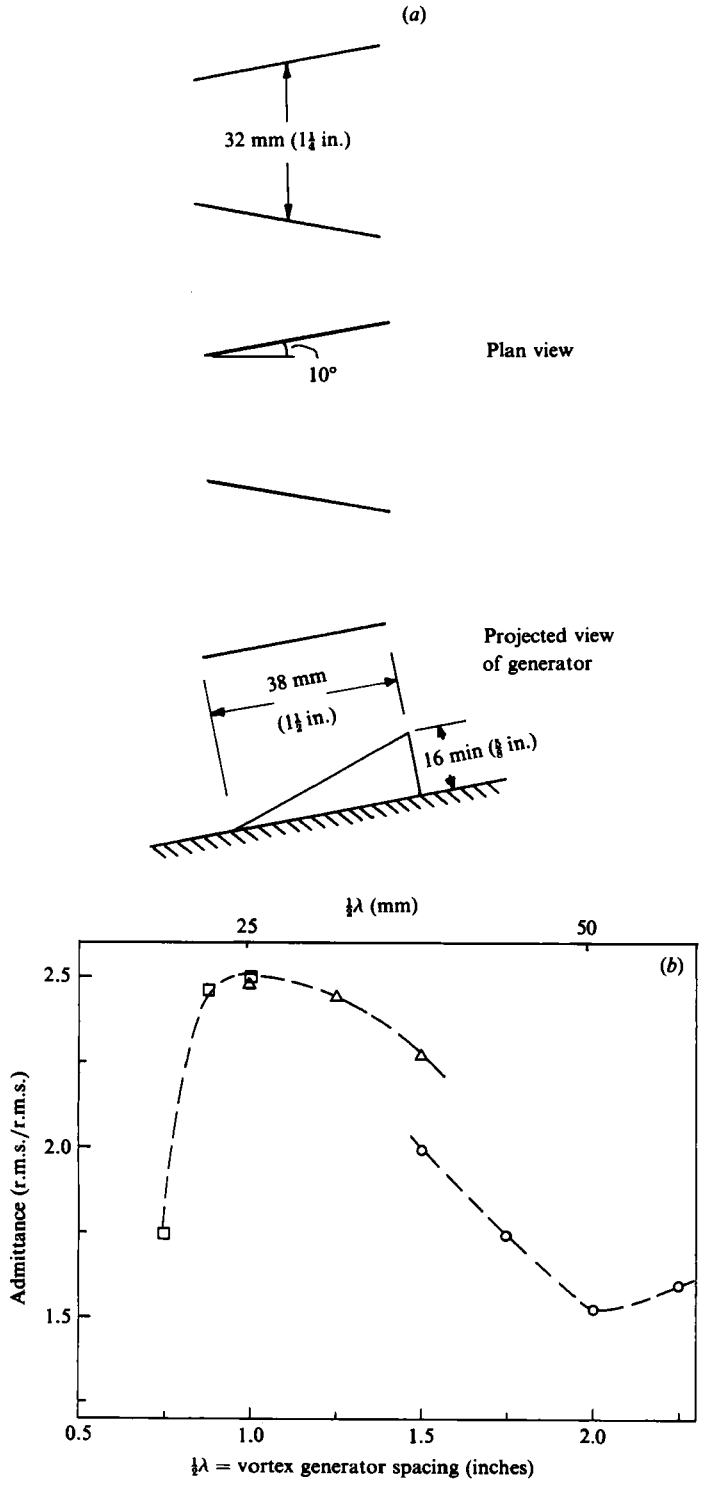

FIGURE 1. Vortex generators. (*a*) Arrangement of vortex generators on floor of settling chamber. (*b*) 'Admittance' (ratio of r.m.s. skin-friction variation at end of curved section to that at start of curved section) plotted against vortex-generator spacing. Different symbols denote different generator sizes.

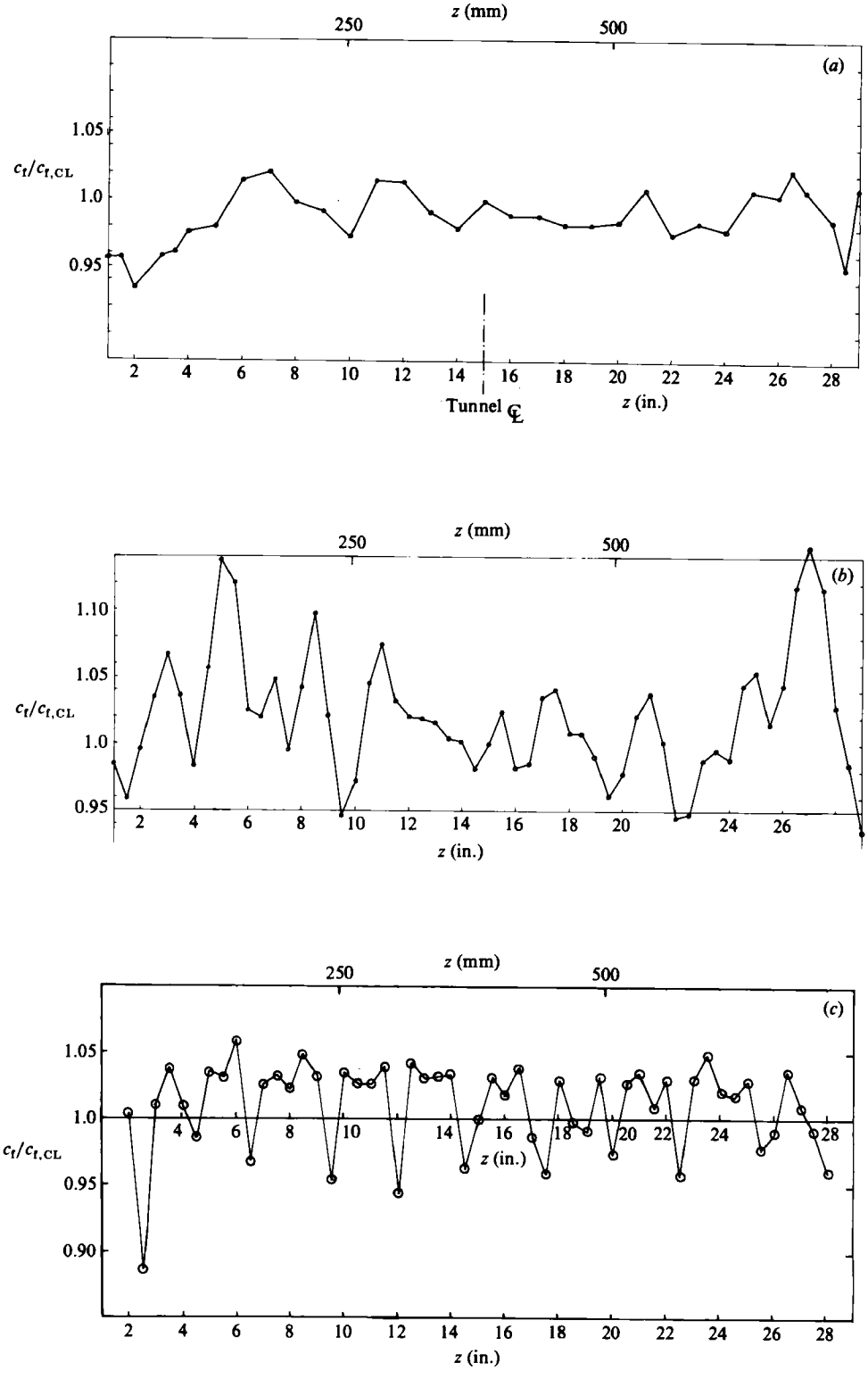

FIGURE 2(*a–c*). For caption see facing page.

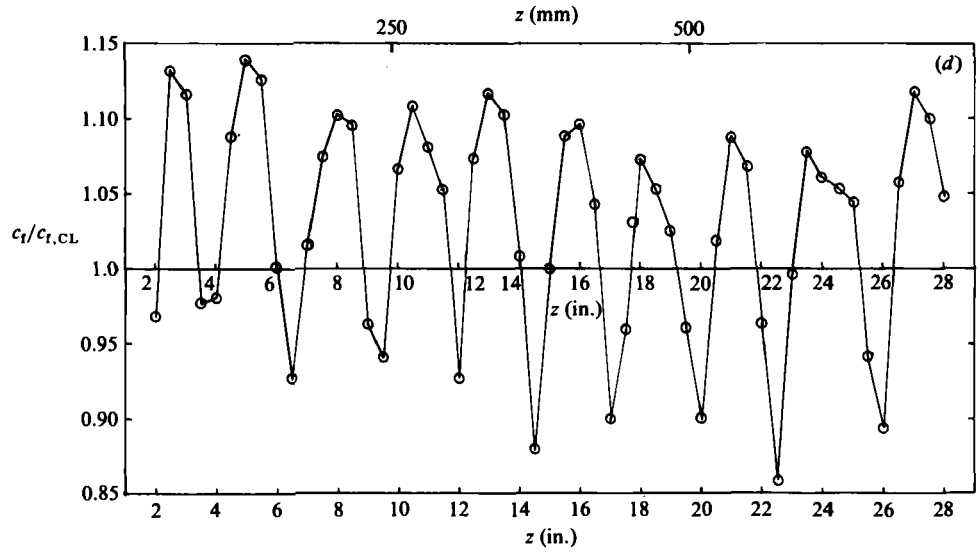

FIGURE 2. Spanwise variation of skin friction (z measured from tunnel sidewall). (*a*) $x = 0$ (start of curved section) without vortex generators. (*b*) $x = 1050$ mm without vortex generators. (*c*) $x = 0$ with vortex generators in settling chamber at 32 mm (1.25 in.) spacing. (*d*) $x = 1050$ mm with vortex generators.

curvature on a turbulent boundary layer are quite different, even qualitatively. This implies that turbulent-flow calculation methods should use quantitatively or even qualitatively different curvature-correction formulae for the stabilizing and destabilizing cases.

Configurations like the present one, in which a well-developed boundary layer suddenly encounters a region of curvature, can be used to investigate both the transient and the asymptotic responses of the turbulence to curvature. Our pair of closely related experiments confirms the implication of previous work that the speed of transient response to stabilizing curvature is much greater than the speed of response to destabilizing curvature. This is understandable once one realizes that stabilizing curvature merely attenuates the existing eddies, while destabilizing curvature results in the quasi-inviscid growth of longitudinal vortices, whose strength is limited only by the opposing Reynolds-stress gradients they generate.

Like I, the companion paper on the convex case, the present paper contains some conditional-sampling measurements, particularly to investigate the effects of curvature on the intermittency factor, and also extensive triple-product measurements. Turbulent transport of Reynolds stress is effected mainly by the large eddies, and appears as triple-product terms in the stress-transport equations: triple-product measurements therefore throw useful light on the large eddies and on transport-equation modelling.

2. Apparatus and techniques

The measurements were made in two stages. Vortex-generator development and mapping of the flow in two cross-sectional planes are reported by Hoffmann & Bradshaw (1981): to illustrate streamwise trends, more detailed measurements at several streamwise stations – but only two spanwise positions – were carried out by

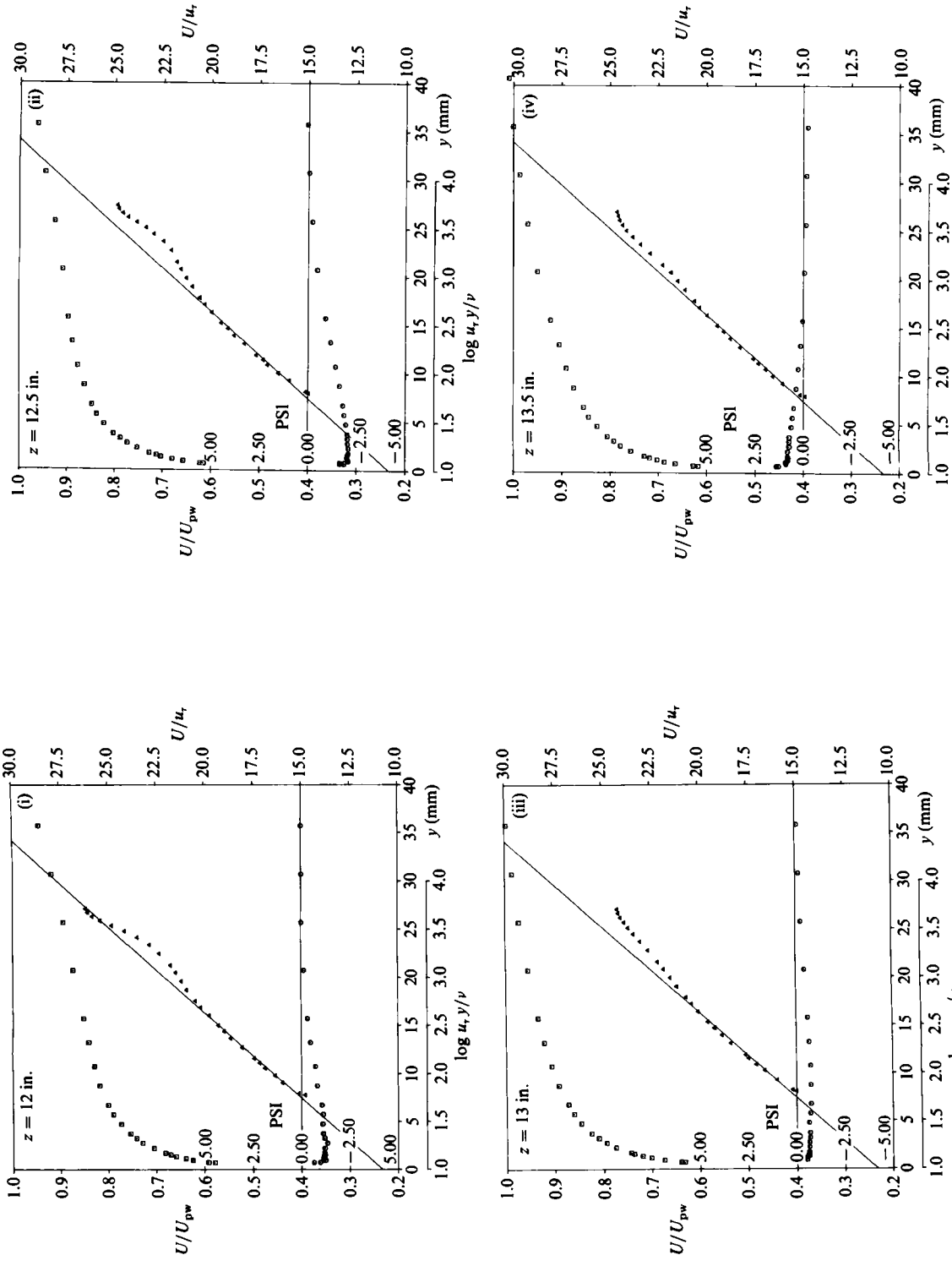

FIGURE 3 (*a*). For caption see page 380.

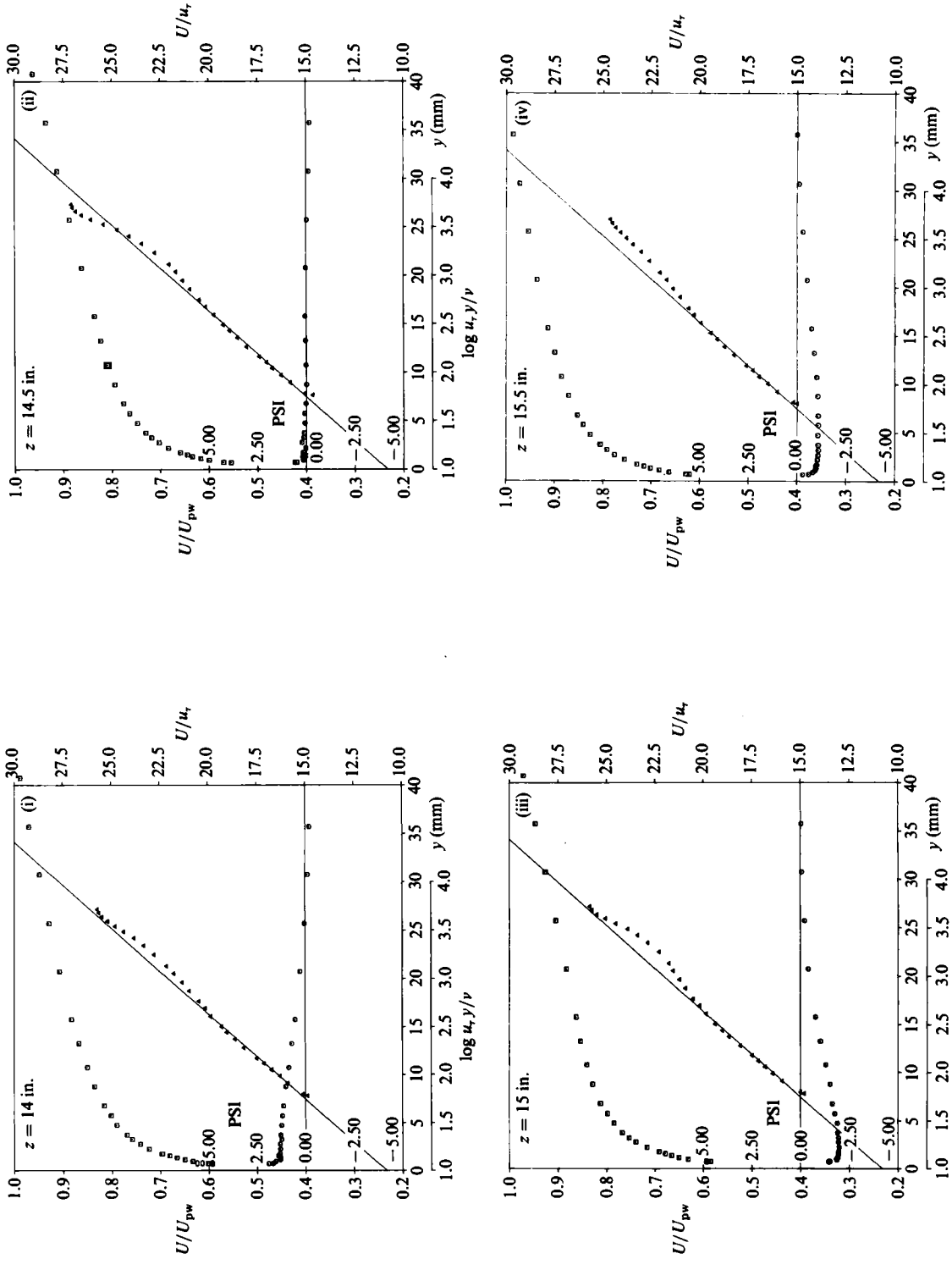

FIGURE 3(*b*). For caption see page 380.

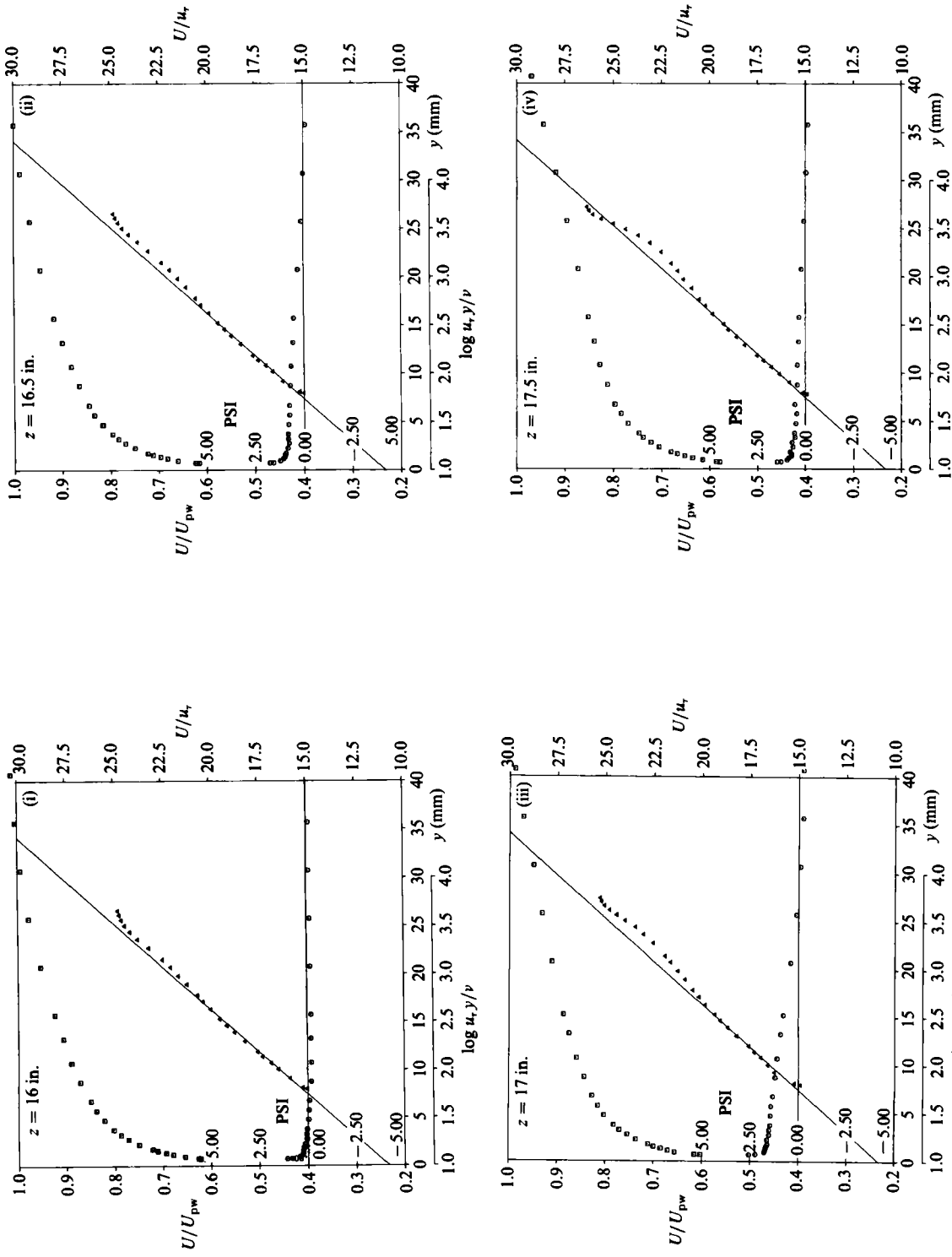

FIGURE 3(c). For caption see page 380.

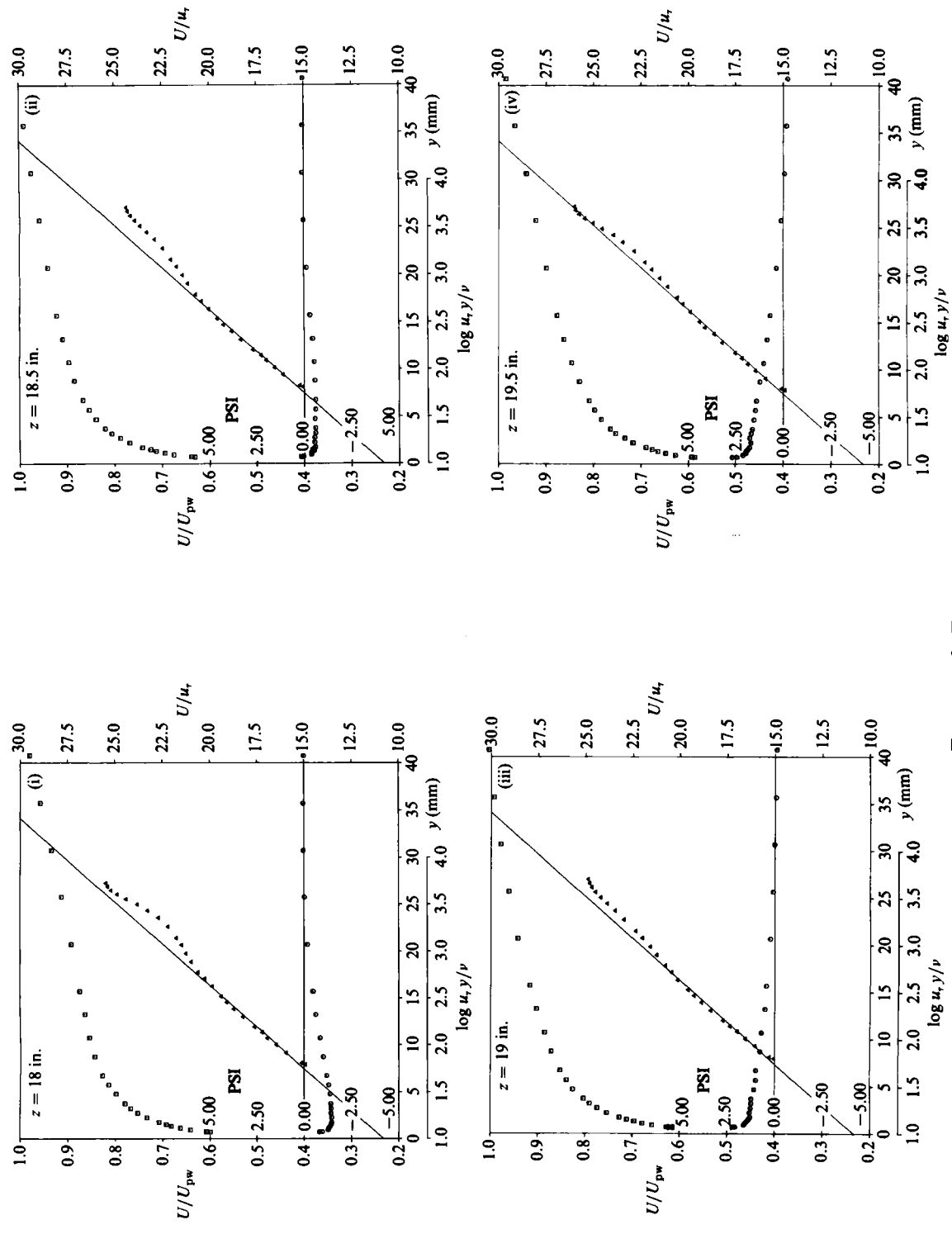

FIGURE 3(*d*). For caption see page 380.

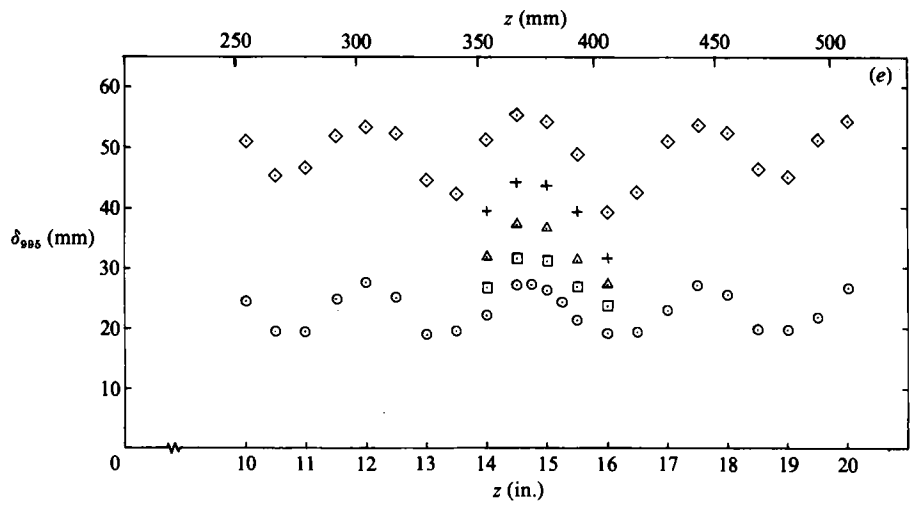

FIGURE 3. Mean-velocity profiles: inclined line is logarithmic law for flat surface, $U/u_\tau = (1/0.41)\ln(u_\tau y/\nu)+5.2$: U_{pw}, potential velocity; u_τ, friction velocity; $\psi°$, yaw angle; □, U/U_{pw} *vs* y; △, U/U_τ *vs* $u_\tau y/\nu$. (*a*) $x = 1050$ mm, $z = 12$–13.5 in. (305–343 mm). (*b*) $x = 1050$ mm, $z = 14$–15.5 in. (356–394 mm). (*c*) $x = 1050$ mm, $z = 16$–17.5 in. (406–444 mm). (*d*) $x = 1050$ mm, $z = 18$–19.5 in. (457–495 mm). (*e*) Variation of boundary-layer thickness with z: ⊙, $x = 0$; ⊡, 90; △, 410; +, 730; ◇, 1050 mm.

Muck (1982). The test rig and techniques are generally as described in I. The working section was 762 mm wide and 127 mm high throughout, with a straight entry section 1450 mm long preceding a curved section whose concave surface had a radius of curvature of 2540 mm. The flow speed at the start of the working section was about 33 m s^{-1}, increasing slightly down the length of the working section owing to boundary-layer growth: the pressure coefficient on both surfaces is shown in figure 1 (*b*) of I.

Conventional hot-wire techniques were used: Muck used DISA 55D01 constant-temperature hot-wire anemometers, while Hoffmann used the Imperial College version of the University of Melbourne hot-wire anemometer. In both cases fluctuating signals from the probe were recorded on analog magnetic tapes, and later transcribed to digital magnetic tape for batch processing, including linearization, on the Imperial College computer. The major difference in technique from that used in I was the need to measure mean products involving both v- and w-component fluctuations in the three-dimensional flow. All the double and triple mean products can be deduced from fluctuation records taken with a cross-wire probe rotated about its axis into four positions so that it responds respectively to v, $(v+w)/\sqrt{2}$, w, and $(v-w)/\sqrt{2}$: four separate measurements of u-component statistics could be made, and these agreed very satisfactorily. We estimate that the absolute uncertainty of Reynolds-stress measurement was about 10 %, except for $\overline{vw}$ where the error is likely to have been 15 % or more. Triple-product uncertainty is also estimated as about 15 %. Spanwise variations are of course shown to much better accuracy than absolute values. In the conditional-sampling measurements, a third, temperature-measuring wire, 1 μm in diameter, was attached to the cross-wire probe, most of the results being obtained from runs with the cross-wire probe in the 'v' position and the temperature-

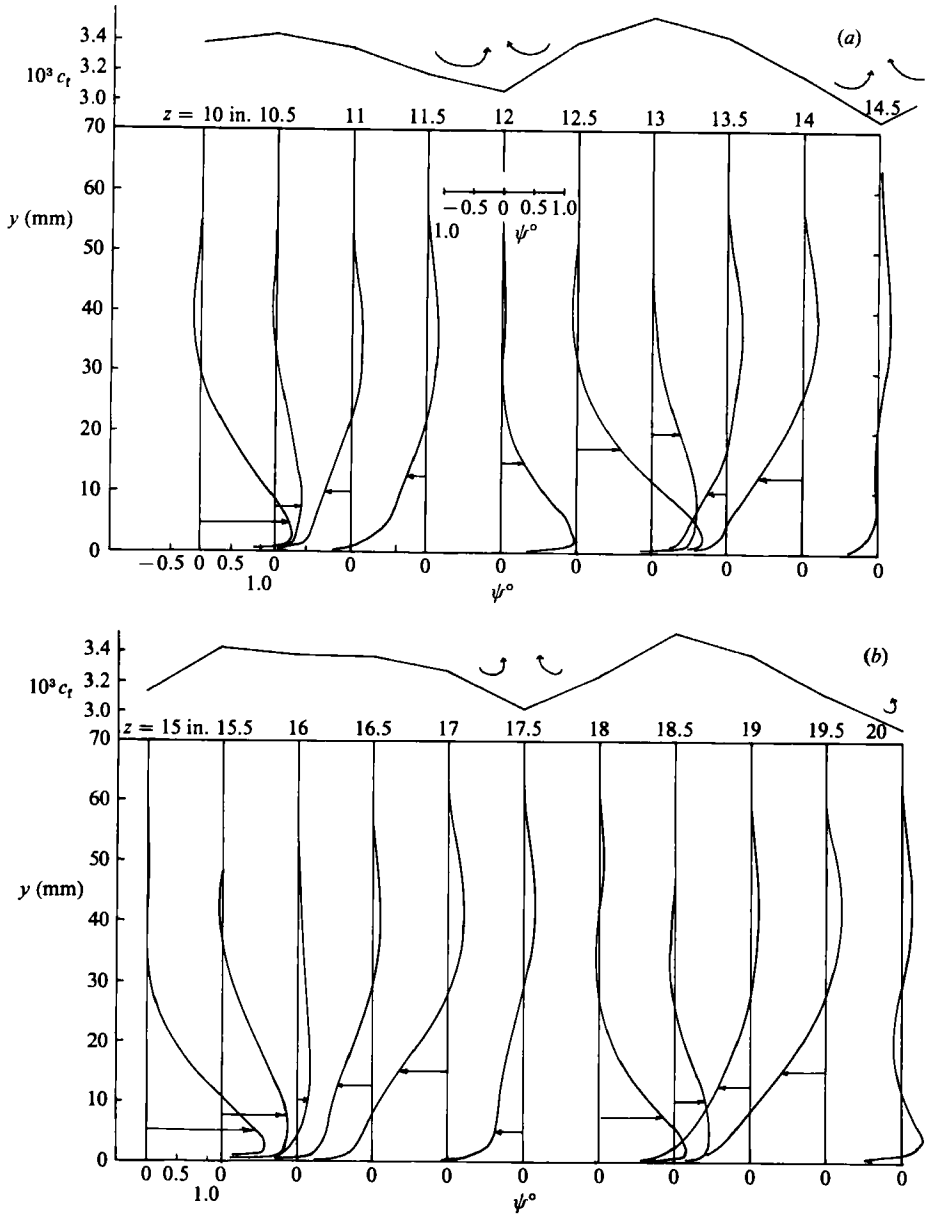

FIGURE 4. Yaw-angle profiles, downstream station (x = 1050 mm). (*a*) $10 < z < 14.5$ in. ($254 < z < 368$ mm). (*b*) $15 < z < 20$ in. ($381 < z < 503$ mm).

measuring wire about one wire length (1 mm) away in the z-direction – i.e. well outside the hot-wire wakes. Yaw-angle measurements were made with three-hole pressure yawmeters, whose readings are more repeatable than those of hot wires, but we did not use the yawmeters for measuring pitch angle because of the spurious pitch reading induced by the presence of a mean shear.

After a rather long process of trial and error, we chose to trigger the vortex pattern by small half-delta wings, as shown in figure 1 (*a*), mounted in the settling chamber

of the wind tunnel upstream of a 9:1 two-dimensional contraction. The spanwise wavelength was chosen to maximize the vortex strength at the downstream end of the test section (as deduced from the spanwise variation of skin-friction coefficient). Note that the two-dimensional contraction of the wind tunnel leaves the vortex circulation and spacing unchanged, but reduces the longitudinal velocity defect in the vortex-generator wakes. Figure 1 (*b*) shows measurements of the 'admittance', arbitrarily defined as the ratio of the r.m.s. spanwise variation of skin friction at the end of the test section to the r.m.s. value at the beginning of the curvature. Disturbances amplify for all wavelengths tested, but the amplification falls off rapidly if the vortex-generator spacing (i.e. half the wavelength) is less than the boundary-layer thickness at the start of the curved section (about 25 mm), and falls off more slowly as the wavelength increases above the optimum. The admittance data should not be taken to have any general quantitative validity, because the disturbance entering the region of curvature was not a set of pure vortices but the remains of vortices introduced into a flat-surface boundary layer far upstream. However, our parametric studies support the implication of previous measurements that a vortex pattern arising from a broad spectrum of natural disturbances is confined to a rather small range of wavelengths.

Figure 2 shows the spanwise variation of skin friction with and without vortex generators, measured with a 1 mm diameter Preston tube: z is measured from one sidewall, so $z = 15$ in. (381 mm) is the centreline. We shall see below that inner-layer velocity profiles appear to follow the standard law of the wall, so that Preston-tube measurements can be relied on. The amplitude of c_f at the start of the curved section ($x = 0$) and the amplification through the curved section are roughly the same in both cases, but the pattern without vortex generators (figures 2 *a*, *b*) is so irregular that any measurements would be very difficult to use in developing or testing a calculation method. Small differences occurred between the time of Hoffmann's measurements and the later measurements of Muck, but the differences in the region of Muck's measurements were very small and the two sets of results can be taken as compatible.

3. Results

The skin-friction measurements with small vortex generators installed in the settling chamber (figures 2 *c*, *d*) show significant departures from a sinusoidal pattern (in all the z-direction plots presented in this paper the straight lines joining measurement points are an aid to viewing rather than a serious attempt at interpolation). Since the vortex amplitude is limited by some sort of nonlinear process, this is not surprising, and the simulation of Moser & Moin shows a very similar pattern. The boundary-layer thickness roughly doubles over the length of the curved section, so that the ratio of vortex spacing to boundary-layer thickness halves. The admittance data of figure 1 (*b*) suggest that a further decrease in this ratio would strongly reduce the vortex-amplification rate or eliminate alternate pairs of vortices.

Figures 3 (*a*)–(*d*) show mean-velocity profiles at the downstream-most station, $x = 1050$ mm, plotted in semi-logarithmic form. Profiles at the start of curvature are given in I. The mean velocity and the yaw angle are plotted against a linear y-scale in the same graphs; yaw angles are also plotted, to larger scale, in figure 4. Figure 3 (*e*) shows δ_{995}, the boundary-layer thickness up to the point where $U/U_e = 0.995$. As in I, the static pressure within the flow was deduced from surface readings by assuming that all streamlines had the same curvature as the surface: velocities are deduced from the local total pressure and the calculated static pressure, and

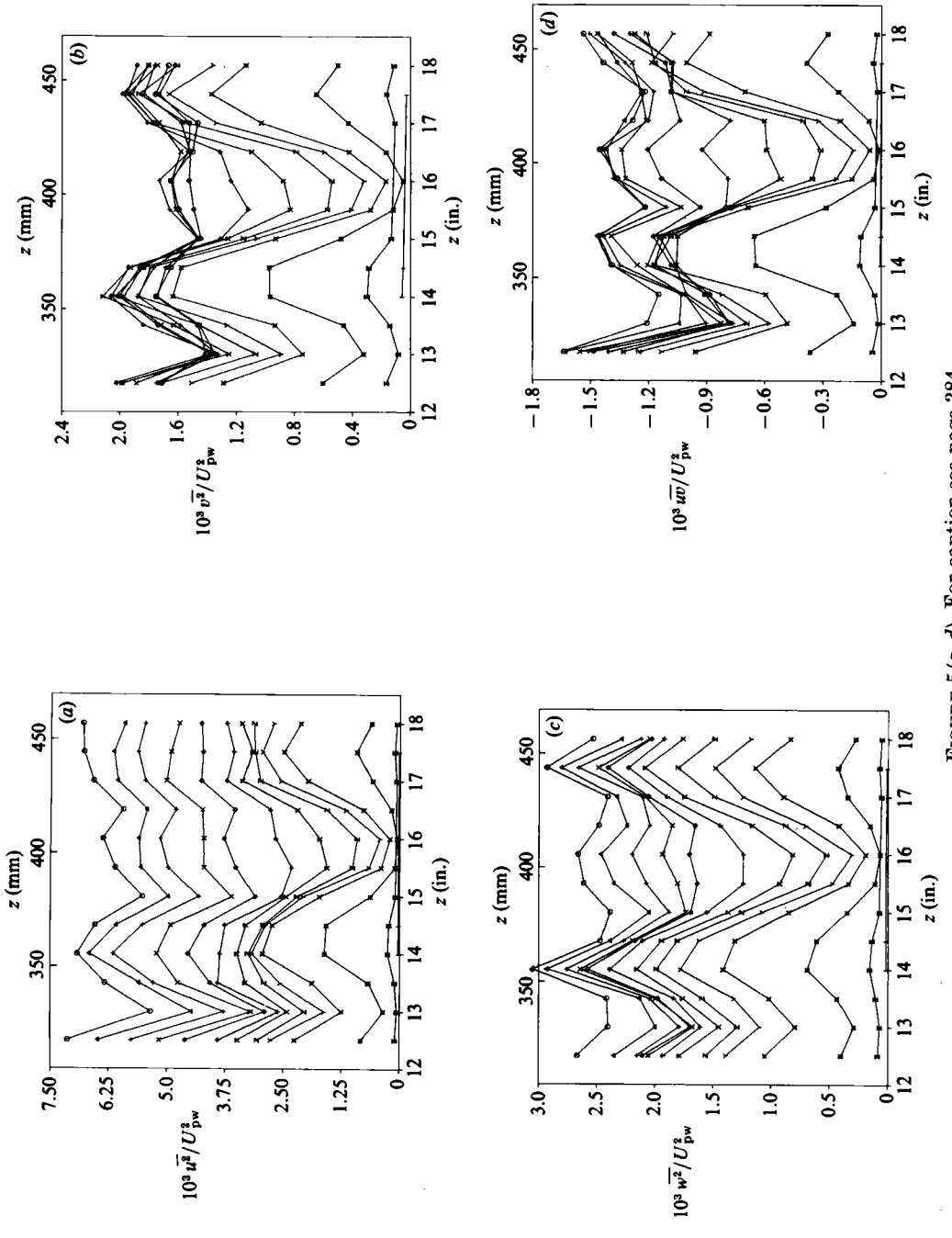

FIGURE 5(*a–d*). For caption see page 384.

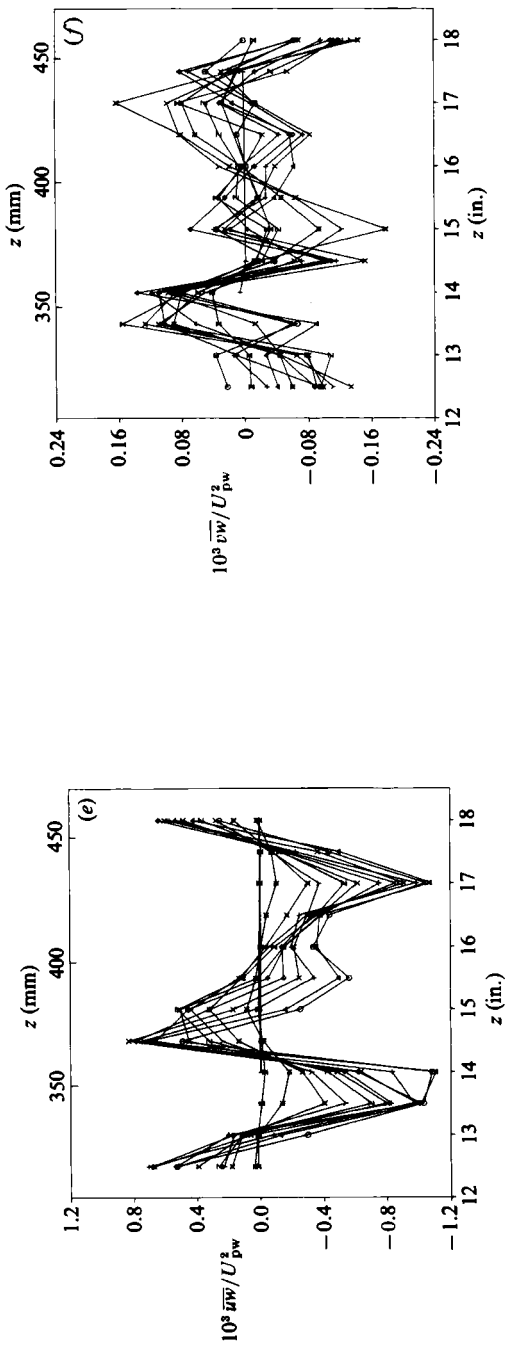

FIGURE 5. Constant-y plots of Reynolds stresses, $x = 1050$ mm. Values of y, mm: ⊙, 4.30; △, 6.20; +, 8.19; ×, 11.2; ◇, 14.2 △, 19.2; ×, 24.2; Z, 29.2; Y, 34.2; ⊡, 39.2; *, 49.2; x, 59.2; |, 69.2. (*a*) $\overline{u^2}/U_{pw}^2$. (*b*) $\overline{v^2}/U_{pw}^2$. (*c*) $\overline{w^2}/U_{pw}^2$. (*d*) $\overline{uv}/U_{pw}^2$: ⊡, $y = 0$. (*e*) $\overline{uw}/U_{pw}^2$. (*f*) $\overline{vw}/U_{pw}^2$. (*g*) $\overline{uw}/u_\tau^2$ at constant y/δ.

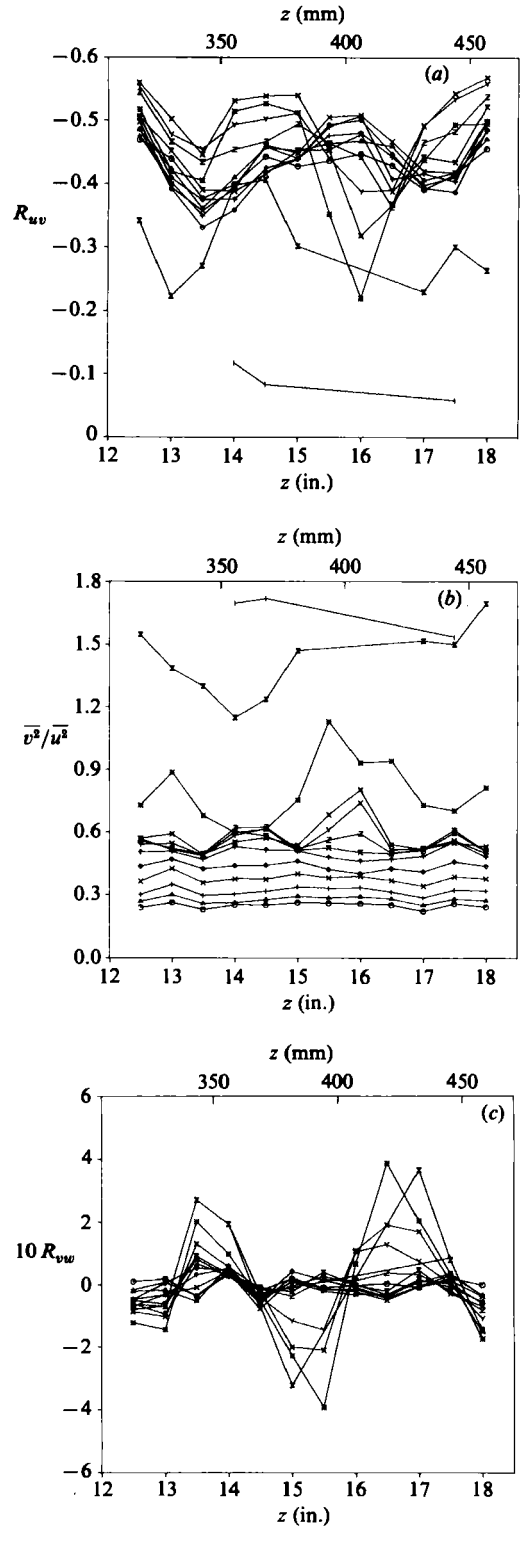

FIGURE 6. Constant-y plots of dimensionless parameters, $x = 1050$ mm: symbols as in figure 5. (*a*) Shear-stress correlation coefficient, $R_{uv} = \overline{uv}/(\overline{u^2}\,\overline{v^2})^{\frac{1}{2}}$. (*b*) $\overline{v^2}/\overline{u^2}$. (*c*) $R_{vw} = \overline{vw}/(\overline{v^2}\,\overline{w^2})^{\frac{1}{2}}$.

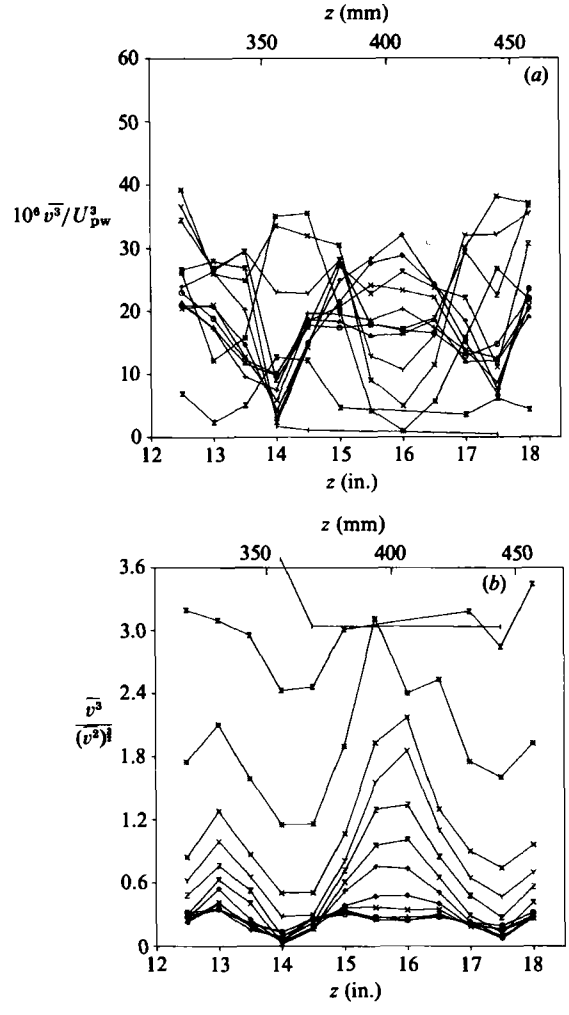

FIGURE 7. Constant-y plots of triple products, $x = 1050$ mm.
(*a*) $\overline{v^3}/U_{pw}^3$. (*b*) v-component skewness, $\overline{v^3}/(\overline{v^2})^{\frac{3}{2}}$.

normalized by the 'potential velocity' at the wall U_{pw} deduced from the free-stream total pressure and the surface static pressure.

Nearly all the mean-velocity profiles at the downstream station, $x = 1050$ mm, have negative 'wake components' – i.e. the profile never rises above the logarithmic law. (The longitudinal pressure gradient induced by boundary-layer growth is far too small to account for this.) Spanwise differences in the profiles between the 'crest' and 'trough' (maxima and minima of $c_f(z)$), say $z = 16$ in. (406 mm) and $z = 14.5$ in. (368 mm) respectively, are somewhat smaller than the average difference between the present results and a typical plane-surface boundary-layer profile, in which U rises above the log law by about $2.5u_\tau$. This suggests that much of the difference between curved-surface and flat-surface velocity profiles is attributable to direct effects of the curvature on the turbulence, but that some of it – the z-dependent part, roughly speaking – is specifically due to the vortex pattern and the secondary effects of the vortex pattern on the turbulence. As in I, we regard the substantial logarithmic region near the surface as an adequate demonstration that the velocity profile follows the

true logarithmic law despite the influences of crossflow and curvature, and we have found good agreement between skin-friction values from logarithmic profile fits and values from Preston tubes (using the calibration of Patel 1965) which rely on log-law universality.

The reason for the dip below the logarithmic law at the outer edge of the inner layer is that destabilizing curvature increases turbulent mixing, reducing the velocity difference between points at different distances from the surface. Spanwise variations of integral parameters, such as displacement thickness and momentum thickness, are tabulated by Hoffmann & Bradshaw and will not be repeated here: the ratio of maximum to minimum boundary-layer thickness at the last test station, $x = 1050$ mm, was about 1.4, and H ranged between 1.211 and 1.268 at the same station. The 'flat-plate' value of H for the same average momentum-thickness Reynolds number, 9000, is 1.33, with $c_f = 0.00267$, but a better comparison would be based on $U_e \delta_{995}/\nu$, which is about 115000 implying a flat plate c_f of 0.0024 (e.g. Andreopoulos & Bradshaw 1980). The spanwise average c_f at $x = 1050$ mm is 0.0033.

Figures 4(*a*) and (*b*) are replots of the yaw-angle measurements, with the skin-friction pattern superimposed for reference, and give a clear idea of the vortex pattern. (The excursions towards negative yaw angle very close to the surface are almost certainly due to slight asymmetry in the yawmeter, leading to errors in yaw angle where $\partial U/\partial y$ is large.) Yaw angles are largest near the surface, comparatively small in the outer part of the flow, and immeasurably small in the external stream. Since the boundary layer is growing in thickness and the vortices are growing in amplitude, the z-wise volume flow rate $\int W \, dy$ need not be zero at any given spanwise station: a detailed study of the critical points in the crossflow plane has been made by Watmuff, Witt & Joubert (1985).

Turbulence measurements are presented in detail by Hoffmann & Bradshaw and by Muck, and only a selection is given here. Most of the present plots show variations with z at constant y at the station furthest downstream ($x = 150$ mm) as the main feature of qualitative interest: $y = 49.2$ mm is close to the *average* boundary-layer thickness at $x = 1050$ mm (see figure 3*e*). Points are joined with straight lines simply as an aid to viewing. The variations can be partly attributed to the spanwise variations of boundary-layer thickness, but there are real structural variations at constant y/δ as well. Quantitative data are best obtained from the above mentioned papers or from magnetic tapes: both are available from the authors.

Figures 5(*a*)–(*f*) show Reynolds-stress measurements at $x = 1050$ mm. The $\overline{uv}$ measurements in figure 5(*d*) show particularly large spanwise changes, with shapes ranging from steep monotonic descents to profiles, at the 'troughs' in c_f, which have secondary peaks as far out as $y/\delta = 0.6$. Surface values are expected to be anticorrelated with values at large y, and the correlation changes sign somewhere inside the first measurement line at $y = 4.3$ mm or less than 0.1δ. This deep penetration of outer-layer trends (due in part to the vortices) into the inner layer is reflected in the logarithmic-law perturbations mentioned above and in the structural changes described below. Figure 5(*g*) shows $\overline{uv}$ at constant y/δ, normalized by the surface shear stress: spanwise variations are of course *stronger* than in figure 5(*d*) because the surface shear stress is in antiphase with the shear stress outside $y/\delta = 0.1$. Figure 6(*a*) shows the shear correlation coefficient R_{uv} (which tends to 0/0 near the edge of the boundary layer so that results are necessarily erratic there). Values near the 'troughs' in c_f are rather larger than the classical figure of about 0.45 found over most of the thickness of a plane boundary layer; there are again very significant spanwise variations, in phase with those of $-\overline{uv}$, which would not be removed by

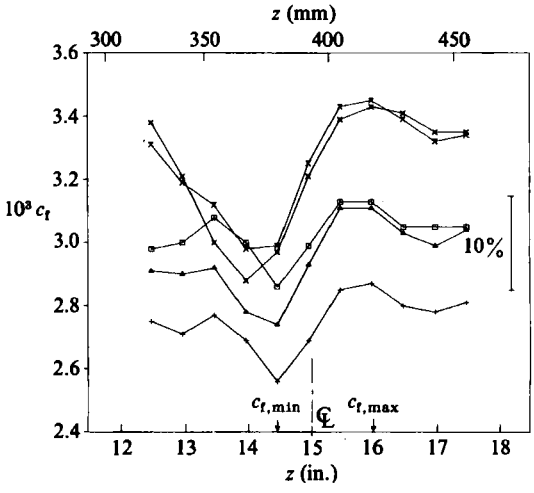

FIGURE 8. Spanwise variation of skin-friction coefficient c_f.

any change of y-scaling. That is, there are changes in the dimensionless structure parameters of the turbulence, of the same order as changes in the Reynolds stresses themselves: calculation methods in which structural parameters like R_{uv} or the stress/energy ratio were assumed constant would not be able to represent spanwise variations accurately. The ratio $\overline{v^2}/\overline{u^2}$, plotted at constant y in figure 6(b), is much less eventful than R_{uv} except near the outer edge, where it rises towards the value of about 2 expected in the irrotational flow: the spanwise variations near the edge are mainly attributable to the variation of boundary-layer thickness, while in mid-layer, $30 < y < 40$ mm, $\overline{v^2}/\overline{u^2}$ tends to be large at maxima or minima of δ – i.e. where the mean V is large in either sense. Muck found a decrease in $\overline{v^2}/\overline{u^2}$ near the outer edge of his convex-surface flow. Figure 6(c) shows R_{vw}, which is small except near the edge, where it shows, more clearly than $\overline{vw}$ itself, a correlation with $\mathrm{d}\delta/\mathrm{d}z$, as expected if $\overline{vw}$ is generated by the $\partial W/\partial y$ set up by the vortex pattern.

The triple products exhibit enormous – but self-consistent – spanwise variations. As a typical example, figure 7(a) shows $\overline{v^3}$, while figure 7(b) shows the more comprehensible variation of the v-component skewness. As in the case of dimensionless second-order parameters like R_{uv}, part but not all of the trend is attributable to spanwise variations of boundary-layer thickness: indeed the latter variations are partly *caused* by increased turbulent transport by triple products – at given y/δ, say – near the maxima of $\delta(z)$.

Mapping of a large number of streamwise stations in the amount of detail shown above for the 'downstream' station would have been excessively time consuming, and two spanwise positions were selected for further measurements, reported in detail by Muck, to fill in the streamwise trends. These positions were close to the 'crests' and 'troughs' in c_f, as indicated in figure 8. Note that at extrema of c_f the crossflow angle and all mean products of fluctuations involving odd powers of w should be zero by symmetry: however, measurements of all fluctuations were made, for the record. Figure 8 shows the skin-friction coefficient for each streamwise position over a short range of spanwise distance only, while figure 9 shows the streamwise variation of the shape parameter H and the wake parameter Π for the 'crest' and 'trough' values of z indicated in figure 8.

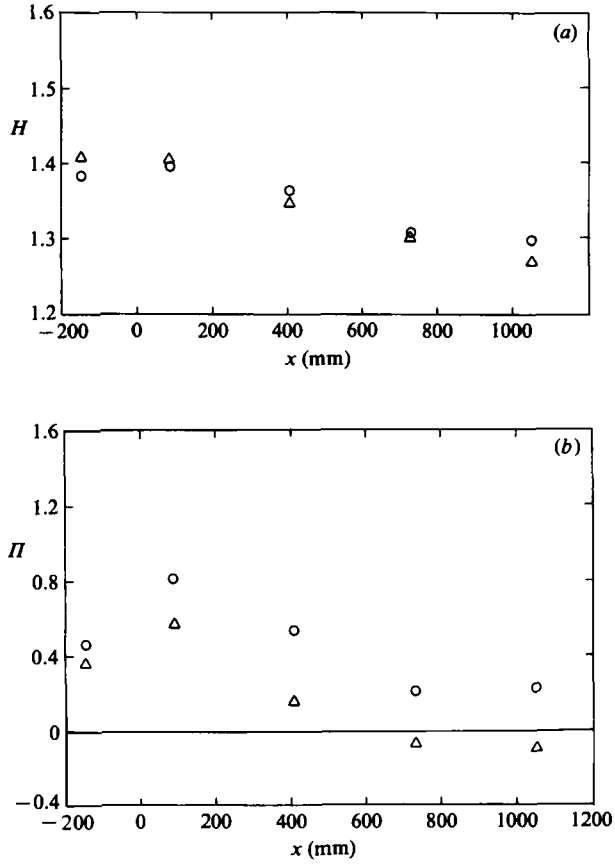

FIGURE 9. Streamwise development of shape parameters. △, $c_{f,\max}$ ('crest'); ○, $c_{f,\min}$ ('trough'). (*a*) Shape factor H. (*b*) Wake parameter Π.

Streamwise trends are sufficiently nearly monotonic for conventional plots against y/δ to be comprehensible. Figure 10(*a*) shows shear-stress profiles for 'crest' and 'trough' positions, together with surface values obtained from logarithmic-law plots. The development of secondary peaks in the shear-stress profiles with increasing downstream distance is clearly seen. It can be plausibly explained as the larger effect of curvature on the larger, outer layer, eddies, but it seems improbable that the double-peak shape will persist indefinitely, since the shear-stress gradient sets up accelerations tending to reduce itself via changes in $\partial U/\partial y$. The conclusion is that the boundary layer at the last measurement station, 50 boundary-layer thicknesses from the start of curvature, is still in a state of transient response to the change in curvature. In the case of convex (stabilizing) curvature (I) readjustment appeared to be effectively complete about 15 boundary-layer thicknesses after the start of curvature. However, it should be noted that δ/R, which is a crude measure of curvature effects, increases much more rapidly on the concave wall than on the convex wall. Figure 10(*b*) shows quite spectacular increases in the stress/energy ratio, which again appear to be continuing strongly at the last measurement station. Figure 10(*c*) shows the shear correlation coefficient, whose trend is similar but somewhat less spectacular (see also figure 6*a*). The difference between the behaviour of a_1 and R_{uv} is explained by the rather significant streamwise increase in $\overline{v^2}/\overline{u^2}$ shown in figure 10(*d*)

($\overline{w^2}/\overline{u^2}$ shows only a slight increase). Recall from figure 6(*b*) that spanwise variations in $\overline{v^2}/\overline{u^2}$ at constant y/δ were fairly small, and recall from I that $\overline{v^2}/\overline{u^2}$ did *not* decrease very significantly in the case of stabilizing curvature. Figure 10(*e*) shows the apparent mixing length, $l = (-\overline{uv})^{\frac{1}{2}}/(\partial U/\partial y)$: although this is not a true turbulence parameter it is a measure of turbulent activity in a given velocity gradient, and, as is well known, it is greatly increased by destabilizing curvature, roughly proportional to the 'Richardson number' $2(U/R)/(\partial U/\partial y)$ if the curvature is prolonged. The differences between the crest and trough positions are qualitatively in agreement with changes in Richardson number due to changes in $\partial U/\partial y$. Figure 10(*f*) shows the eddy viscosity $(-\overline{uv})/(\partial U/\partial y)$ normalized in the usual way. Peak values in the upstream boundary layer are close to the classical 0.0168: the increase downstream is larger than for mixing length simply because $-\overline{uv}$ appears in the latter only in a square root.

Figure 11 shows the streamwise development of $\overline{uv^2}$, whose y-direction gradient appears as the turbulent transport term in the $\overline{uv}$-transport equation and whose spanwise variation is similar to that of $\overline{v^3}$ (figure 7). Very large streamwise changes are seen, with a general increase in triple product with increasing x but a decrease to negative values near the wall at the 'trough' position. The very large difference between the 'crest' and 'trough' values near the wall is presumably a response to the spanwise $\overline{uv}$-gradient imposed by the secondary flow. Plots of the other triple products are given by Muck and show the same general streamwise trends. The 'bulk transport velocities' V_q and V_τ are defined as

$$V_q = \frac{\overline{u^2v} + \overline{v^3} + \overline{vw^2}}{\overline{u^2} + \overline{v^2} + \overline{w^2}}, \tag{1}$$

$$V_\tau = \frac{\overline{uv^2}}{\overline{uv}}, \tag{2}$$

neglecting transport by pressure fluctuations in each case, and are shown in figures 11(*b*), (*c*) respectively. They show somewhat less spectacular variations than the raw triple products although percentage differences in the 'crest' and 'trough' values near the wall are still extremely large. Over the layer as a whole, the percentage changes in V_τ with streamwise distance are very much less than the changes in V_q. Differences between the 'crest' and 'trough' values in the outer layer are small in both cases, as also shown by the more detailed spanwise plots of Hoffmann & Bradshaw. The ostensible practical conclusion is that a plane-boundary-layer model of shear-stress transport velocity V_τ (but not of V_q) could also be used in curved flows. However, this conclusion does not apply to the boundary layer investigated by Smits, Young & Bradshaw (1979), in which a short region of very strong concave curvature was followed by a flat recovery surface: there, changes in shear-stress transport velocity were large, although again the differences between 'crest' and 'trough' values were most pronounced in the inner layer. (Recall from I that on a convex surface V_q and V_τ decrease significantly only in the outer part of the layer, though in the measurements of Smits *et al.* the transport velocity of turbulent energy fell almost to zero throughout the layer at the end of a region of strong convex curvature.)

Flatness factors of all three velocity components remain near the Gaussian value of 3 in the inner layer, but large increases with x occur in the outer layer, especially in the case of the u-component plotted as 3/(flatness factor) in figure 12. The reason is not immediately obvious: certainly, the intermittency factor γ at a given value of y/δ (figure 13) decreases with increasing x, but – on the usual simple assumption

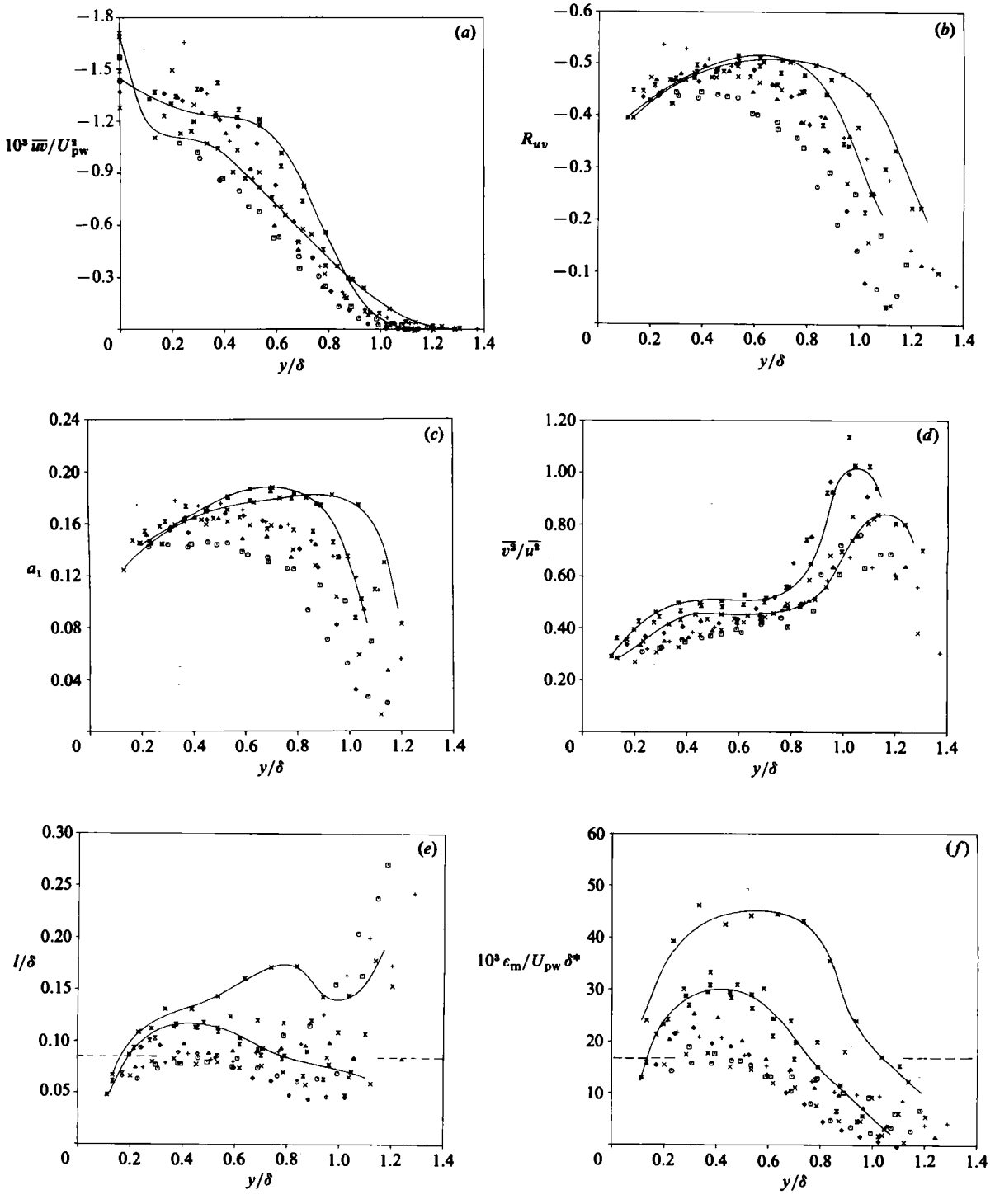

FIGURE 10. Streamwise development of Reynolds stresses. Symbols for $c_{f,\max}$ and $c_{f,\min}$ respectively: □, ○, $x = -145$ mm; +, ×, $x = 90$ mm; △, ◇, $x = 410$ mm, ⧖, ⧗, $x = 730$ mm; —○—, —*—, $x = 1050$ mm. (*a*) Primary shear stress, $10^3(-\overline{uv}/U_{pw}^2)$. (*b*) Shear-stress correlation coefficient, $R_{uv} = \overline{uv}/(\overline{u2}\,\overline{v^2})^{\frac{1}{2}}$. (*c*) Stress/energy ratio, $a_1 = -\overline{uv}/(\overline{u^2}+\overline{v^2}+\overline{w^2})$. (*d*) Ratio of normal stresses, $\overline{v^2}/\overline{u^2}$. (*e*) Prandtl's mixing length for primary shear stress $-\overline{uv}$, l/δ_{995}. (*f*) Eddy viscosity, $\epsilon_m/U_{pw}^3\delta^*$.

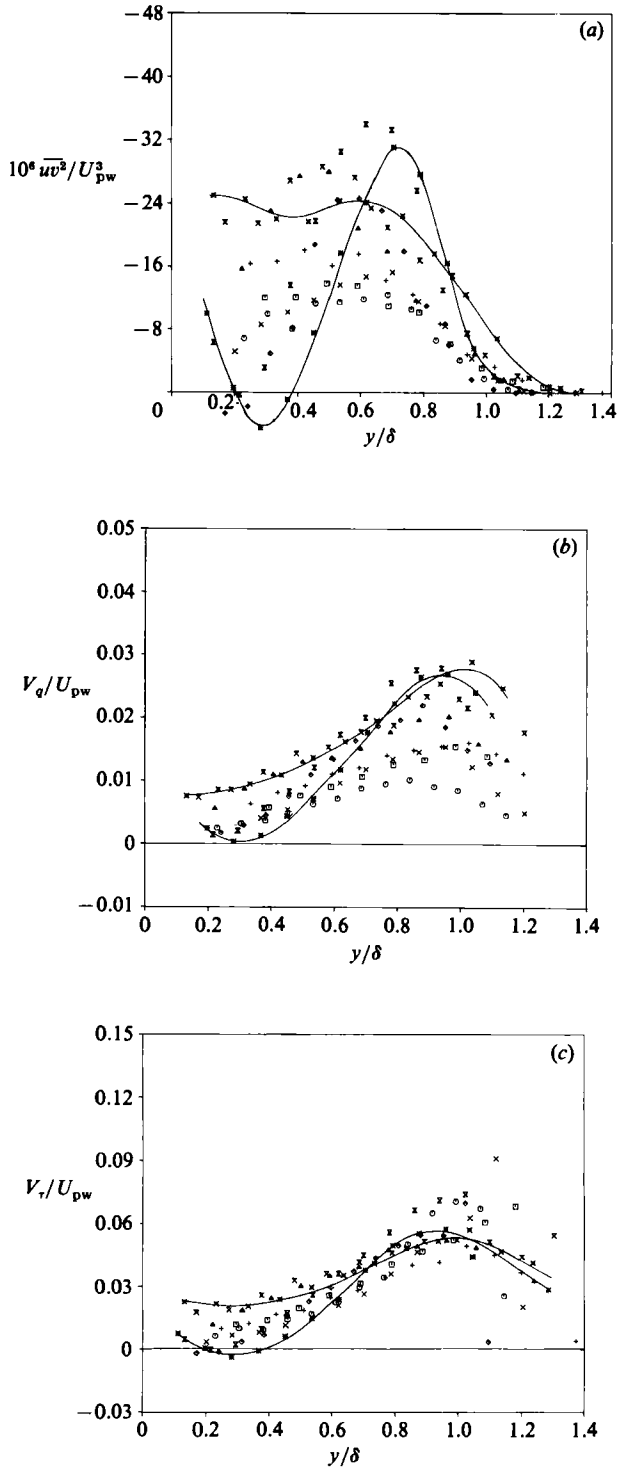

FIGURE 11. Streamwise development of triple products: symbols as in figure 10. (*a*) Triple product $\overline{uv^2}$. (*b*) Transport velocity for turbulent kinetic energy, V_q/U_{pw}. (*c*) Transport velocity for primary shear stress, V_τ/U_{pw}.

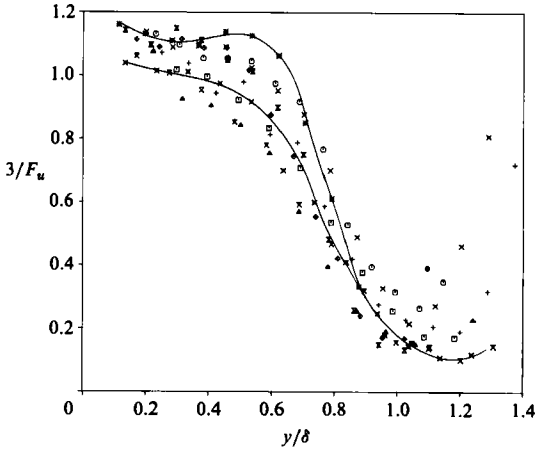

FIGURE 12. u-component flatness factor, $F_u = \overline{u^4}/(\overline{u^2})^2$, symbols as in figure 10.

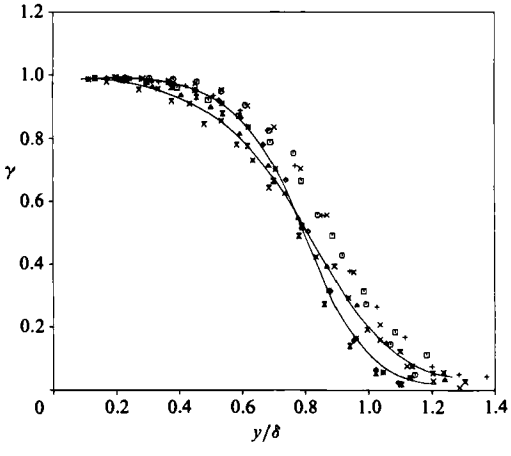

FIGURE 13. Intermittency factor γ, symbols as in figure 10.

that the intermittency is given approximately by 3/(flatness factor) – this would simply translate the flatness-factor curves in the y-direction rather than change the peak values of flatness factor. The effect of the narrowing, with increasing x, of the irrotational core region between the boundary layers on the two curved walls of the test rig would be to *decrease* the measured flatness factor because of near-Gaussian contributions from the opposite boundary layer's irrotational field. The change in the intermittency profiles with x is attributable at least as much to changes in the outer-layer mean-velocity profile, and hence in the relation between δ and the turbulence lengthscales, as to real structural changes. However, the value of y/δ at which intermittency starts to decrease from the fully turbulent value of unity certainly decreases with increasing downstream distance, at both 'crest' and 'trough' positions. Note that small lateral wandering of the vortices does not affect intermittency at the crest and trough where $\mathrm{d}\delta/\mathrm{d}z$ is nominally zero. Intermittency changes in the convex case are much smaller, supporting the general argument that convex curvature mainly attenuates the eddies whereas concave curvature changes their structure.

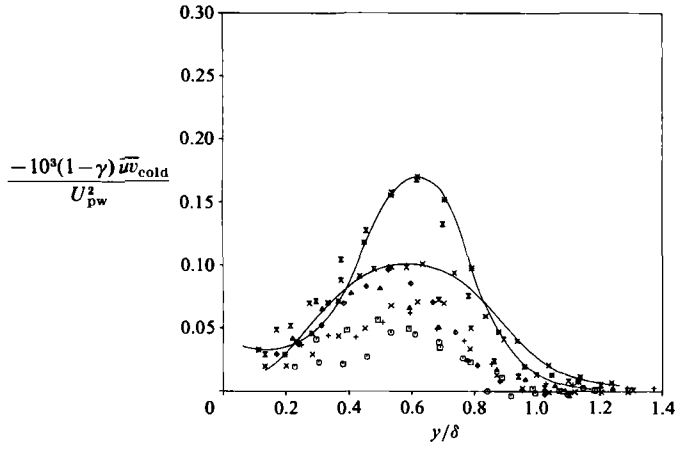

FIGURE 14. Non-turbulent ('cold')-zone contribution to primary shear stress, $-10^3(1-\gamma)\overline{uv}_{\text{C}}/U_{\text{pw}}^2$, symbols as in figure 10.

Conditionally sampled values of all variables for 'turbulent' and 'non-turbulent' (irrotational) regions are given by Muck. As in our previous work, all fluctuations are measured with respect to the conventional-average (mean) velocities, so that for any variable Q the addition law

$$Q = \gamma Q_{\text{H}} + (1-\gamma)\, Q_{\text{C}} \tag{3}$$

applies: here suffix H ('hot') denotes the turbulent zone and suffix C ('cold') the unheated outer irrotational zone. As might be expected, differences between zonal-average velocities (not shown here) and the conventional-mean velocity increase with increasing downstream distance, as the turbulence level rises. The difference between the conventional and turbulent-zone U-component velocities is everywhere small, but the difference between the conventional and *irrotational*-zone average U-component velocity reaches more than 0.05 of the free-stream velocity at $x = 1050$ mm: the fact that the differences are larger near the wall, where the intermittency is nearly unity, suggests that the intermittency-measuring technique is a fairly accurate one, because even small errors near $\gamma = 1$ would greatly reduce the difference between non-turbulent-zone and conventional mean velocities. V-component zone averages also increase with x, particularly the turbulent-zone average which is a measure of the intensity of the large eddies.

Because velocity fluctuations in an irrotational zone are fairly weak, the difference between conventional and turbulent-zone averages of velocity products is small and therefore, as in I, we present only the irrotational-zone averages, from which the turbulent-zone averages can be deduced by using (3). All irrotational-zone averages increase with x much more rapidly than the conventional-zone averages, the peak irrotational contribution to $\overline{uv}$ (figure 14) increasing by a factor of 3 down the length of the working section. The same general conclusion would apply to products of fluctuations about the zonal-average velocity, as well as to the fluctuations about the conventional-average velocity as defined here; the implication is that the irrotational motion becomes substantially better organized as the large eddies gain in intensity, generating stronger eruptions into the irrotational fluid. The irrotational-zone skewness factor and flatness factor provide the best guide to the structure of the irrotational motion, although quantitative values depend greatly on whether the

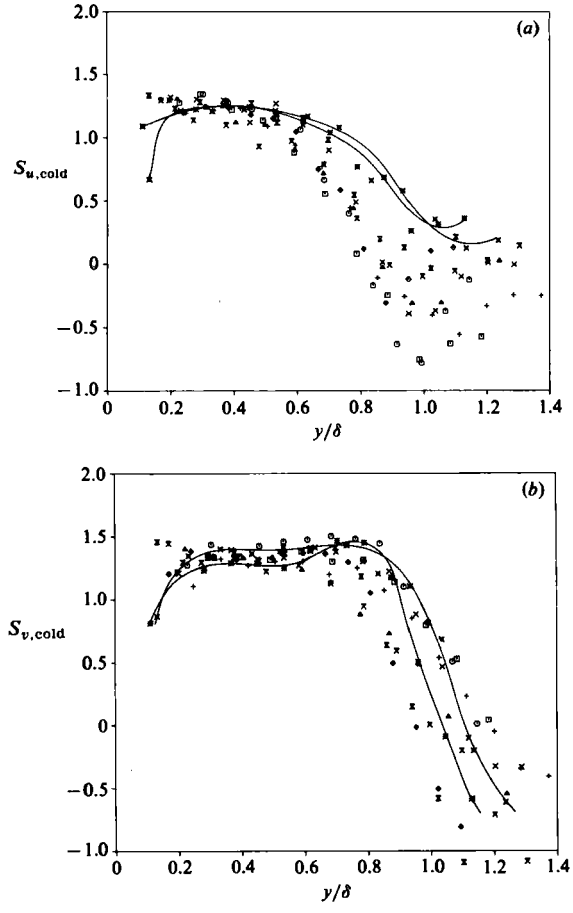

FIGURE 15. Non-turbulent ('cold')-zone skewness factor, symbols as in figure 10. (*a*) $S_u = \overline{u_{\mathrm{C}}^3}/(\overline{u_{\mathrm{C}}^2})^{\frac{3}{2}}$. (*b*) $S_v = \overline{v_{\mathrm{C}}^3}/(\overline{v_{\mathrm{C}}^2})^{\frac{3}{2}}$.

zonal or conventional-average velocity is used as baseline. The variation of u-component irrotational-zone skewness across the layer (figure 15*a*) is greatest at the upstream station, decreasing very considerably as the flow moves downstream: this trend is in the same sense as for the convex case, but much more pronounced. The variation of v-component skewness across the boundary layer increases with x although the results are rather scattered: there is not, of course, any close connection between the irrotational-zone skewness of v and the conventional skewness plotted in figure 7 (*b*), except at the edge of the layer where the turbulence dies out. The irrotational-zone flatness factor of u – not shown here – is significantly less than the Gaussian value of 3 near the wall, and rises in the outer layer to a maximum value which, like the skewness, decreases with increasing x. The v-component flatness factor in the outer layer appears to increase with x and then decrease, again following the behaviour of the skewness. Paradoxically, an increase in activity in the irrotational zone may result in a decrease in the numerical value of the skewness in that zone, at least when the fluctuations are measured from the conventional-average velocity rather than from a zonal-average velocity. For example, if the non-turbulent-zone velocity were constant, the skewness according to the present statistics would be +1,

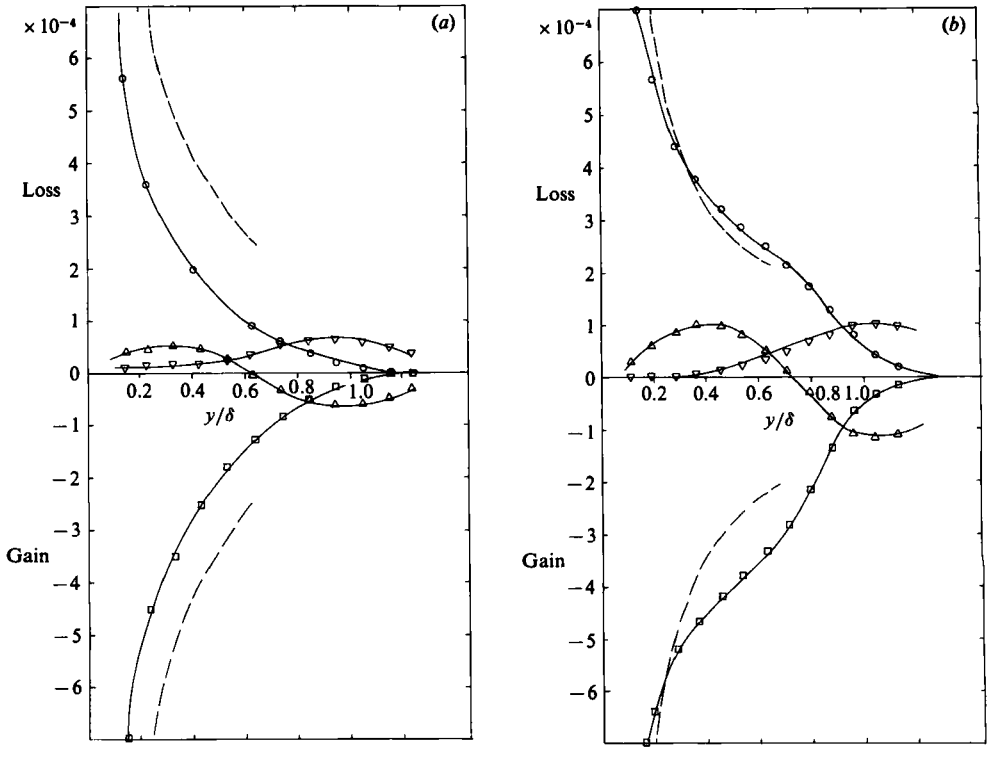

FIGURE 16. Turbulent-energy balance, $x = 1050$ mm (for balance at $x = -143$ mm see I): □, production: ○, dissipation (by difference); ▽, advection; △, diffusion; ---, u_τ^3/Ky. All values normalized by U_{pw}^2/δ. Pressure diffusion neglected. (*a*) 'Crest' ($c_{\mathrm{f,max}}$). (*b*) ('Trough' ($c_{\mathrm{f,min}}$).

while if the amplitude of the fluctuations about the non-turbulent-zone average became large the skewness would gradually tend to the value appropriate to the fluctuation pattern (zero for a symmetrical wave, negative for downgoing spikes).

Figure 16 shows turbulent-energy balances, and figure 17 the *uv*-shear-stress balances, first at $x = -145$ mm on the flat surface, for reference, and then at the 'crest' and 'trough' ($c_{\mathrm{f,max}}$ and $c_{\mathrm{f,min}}$) positions at $x = 1050$ mm. All terms increase with increasing x; the turbulent transport terms increase more in proportion than the 'generation' and 'destruction' terms. Comparison with the results presented in I, figure 15, shows how spectacularly the triple-product transport terms differ between the stable and unstable cases, indicating great differences in the strength of the large eddies relative to the rest of the turbulence. The turbulent-energy dissipation (deduced, as in I, as the net sum of the other terms) has been used to deduce the dissipation-length parameter $L_\tau = (-\overline{uv})^{\frac{3}{2}}/\epsilon$, and the results are shown in figure 18. Again, differences between the concave and convex cases are spectacular, but surprisingly large differences also appear between the 'trough' and 'crest' positions in the concave-surface flow. Recall from figure 16 that the dissipation appears to take unusually large values near the outer edge of the layer at the 'trough' position, where the secondary flow transports fluid outwards from the more highly turbulent regions near the surface.

The on–off intermittency function, whose time average is the intermittency factor γ, has been used to deduce statistical-average lengths of the turbulent and irrotational

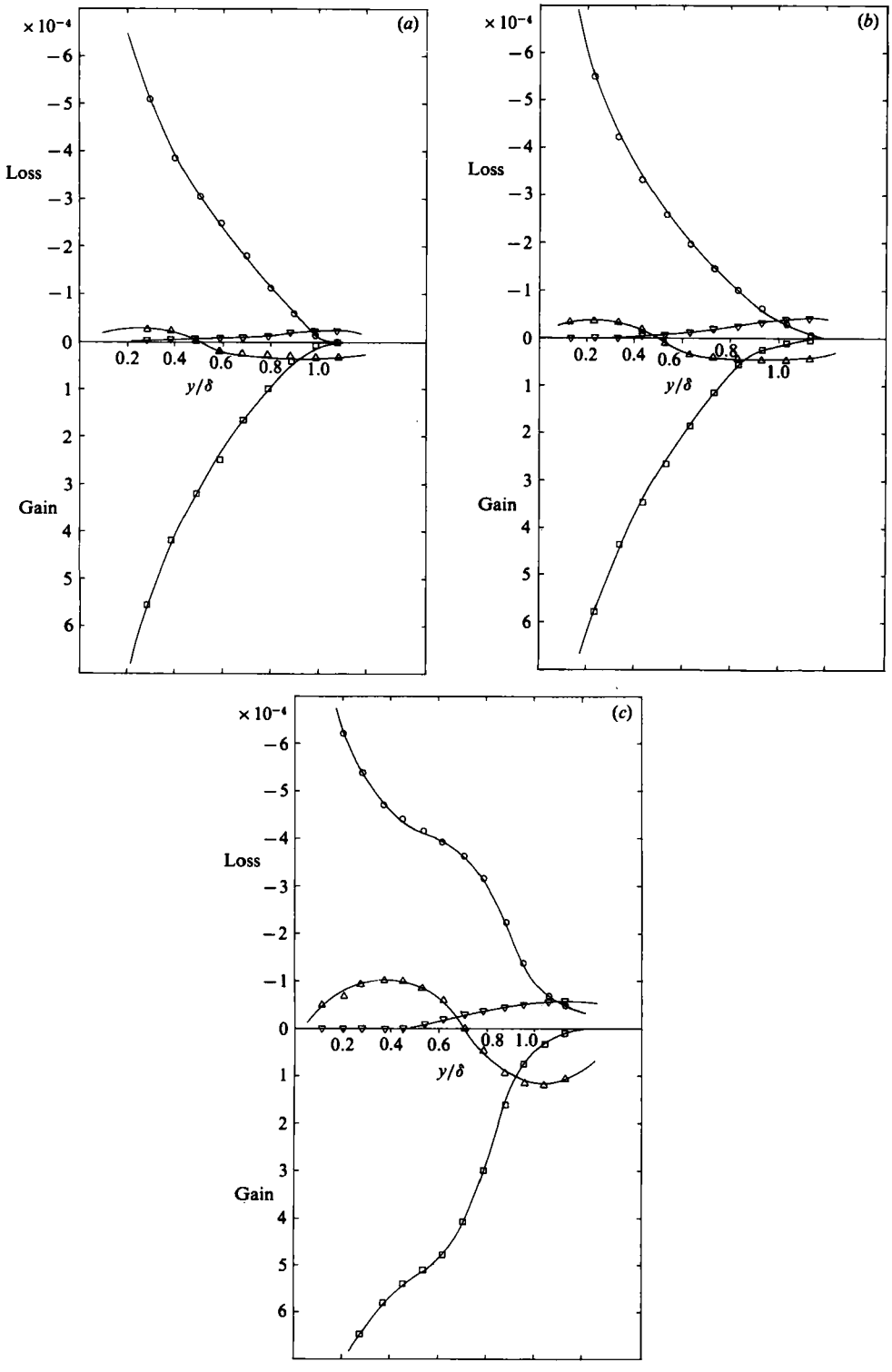

FIGURE 17. Primary shear-stress balance: □, generation; ○, pressure-strain 'redistribution'; ▽, mean transport; △, turbulent transport. (*a*) $x = -143$ mm. (*b*) $x = 1050$ mm, 'crest' ($c_{f,\max}$). (*c*) $x = 1050$ mm, 'trough' ($c_{f,\min}$).

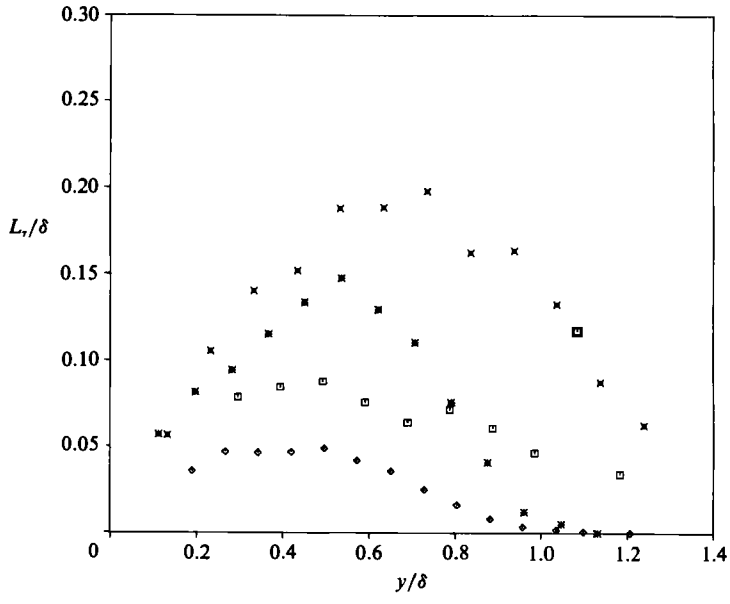

FIGURE 18. Dissipation-length parameter $(-\overline{uv})^{\frac{3}{2}}/\epsilon$. □, $x = -143$ mm; ⌑, $x = 1050$ mm, 'crest'; *, $x = 1050$ mm, 'trough', ◇, $x = 1000$ mm, *convex* surface.

zones. In figure 19, the results are also tabulated against γ, thought to be a more meaningful abscissa than y/δ (see the above presentation of the intermittency-factor results). In these axes, the effects of curvature (convex or concave) appear to be negligible, which is an interesting implication that changes in large-eddy size are small – or at least no larger than changes in the lengthscale of the intermittency-factor distribution.

4. Discussion

The above results confirm and extend the description of turbulent flow given by previous experimental work. Perhaps the most important conclusion is that although spanwise variations in dimensionless turbulence-structure parameters are significant – that is, quasi-steady longitudinal vortices do significantly alter the turbulence structure – these variations are somewhat smaller than the changes from plane-surface structure owing to the direct effects of streamline curvature ('centrifugal force') on the turbulence. We have not tried to explore the circumstances in which vortices are not observable (as in Jeans & Johnston's work, for example) but the above conclusion does imply that any consequent changes in overall behaviour may be comparatively small. Pure amplification of existing eddy structure would leave the dimensionless structure parameters unaltered, so that we must postulate quite significant changes in eddy behaviour. We have not found any evidence that the large eddies tend to become (unsteady) longitudinal vortices themselves: if this happened one would expect noticeable increases in the lengths of turbulent bursts in the outer layer, while figure 19 shows that no significant changes occur. The unsteady sweep and ejection motions observed by Jeans & Johnston would contribute to conventional turbulent averages even though the frequencies seen by a fixed observer are much less than those of the turbulent eddies.

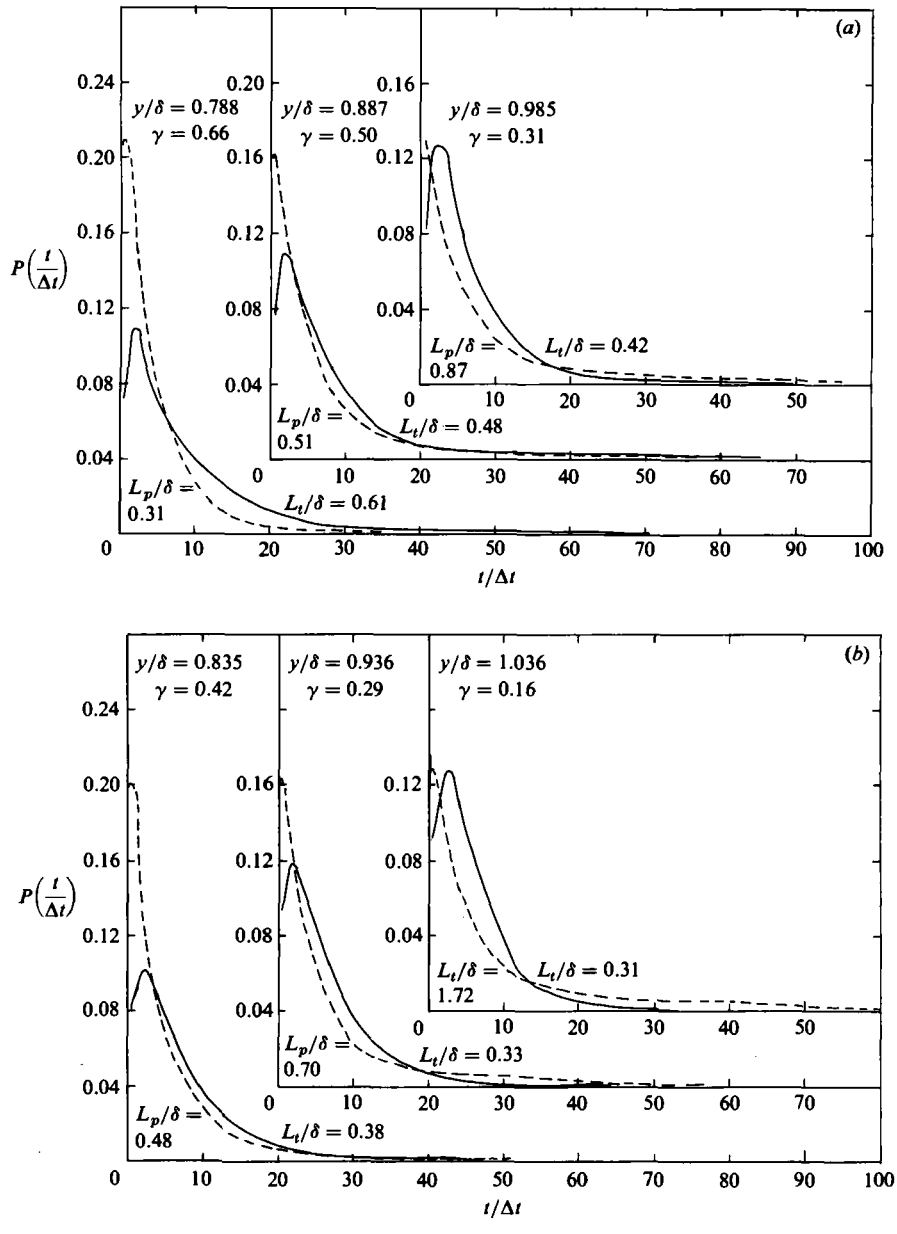

FIGURE 19(*a*,*b*). For caption see page 400.

Vortex unsteadiness need not be considered explicitly in turbulence models for the spanwise-averaged structure, but, whereas it is possible to conceive of a Reynolds-averaged three-dimensional calculation of a flow with fixed vortices, *unsteady* longitudinal vortices and the remainder of the large-eddy pattern could be distinguished computationally only by conditional sampling of time-dependent simulation results. Simulations with an accuracy comparable to that of experiments are now starting to appear for complex flows: the work of Moser & Moin is an example, although the size of their vortices was too strongly constrained by the lateral

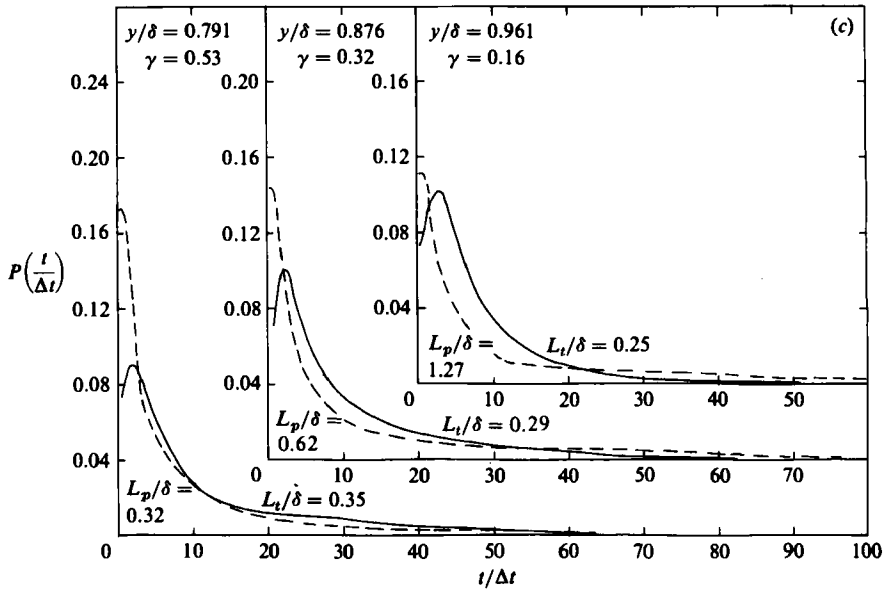

FIGURE 19. Probability distribution of turbulent- and non-turbulent-zone lengths in intermittent region. Time intervals Δt, same for all y, is 37.5 μs: $U_e \Delta t = 1.2$ mm. ——, turbulent zone; – – – potential zone. (*a*) $x = -143$ mm; $U_C \Delta t/\delta \doteq 0.05$. (*b*) $x = 1050$ mm, 'crest' ($c_{t,\max}$); $U_C \Delta t/\delta \doteq 0.03$. (*c*) $x = 1050$ mm, 'trough' ($c_{t,\min}$); $U_C \Delta t/\delta \doteq 0.023$.

boundary conditions for detailed comparison with the present experiments to be profitable. In many practical problems the boundary layer will have pre-existing spanwise non-uniformity, because of the non-uniformity of transition on – say – aircraft wings or turbomachine blades, which usually have significant structural irregularities or impact damage. In some wind-tunnel experiments, such as that of Smits *et al.* in the same tunnel as the present study, spanwise variations were so sharp that the vortex pattern must have been effectively fixed, without appreciable spanwise 'wandering'. In the present case, spanwise variations are sufficiently mild that spanwise wandering, with a tendency for the vortices to prefer certain spanwise positions with a resulting time-average spanwise periodicity, cannot be ruled out entirely, despite the 'fixing' of the pattern by vortex generators: however, there is no trace of the increase in streamwise lengthscales that such wandering would presumably produce. These different cases are to some extent artifacts of our conventional system of taking averages, but more work – perhaps not involving very detailed turbulence measurements – needs to be undertaken to improve our knowledge of the vortices and the conditions for their occurrence.

The general behaviour of the longitudinal-component mean-velocity profiles and of the Reynolds stresses is what would be qualitatively expected from a combination of the presence of (fixed) longitudinal vortices and a general destabilizing effect on the turbulence. For example, the overall effect of curvature on the mean-velocity profile is to reduce the 'wake' component – i.e. the deviation from the logarithmic law – because an increase in turbulent mixing implies a decrease in mean-velocity gradient. The spanwise variations of the mean-velocity profiles are in the sense to be expected from the vertical transport of fluid by the vortices. Percentage changes in the Reynolds stresses are largest in the outer layer, where the ratio of eddy size to radius of curvature is largest. The secondary peaks in some of the Reynolds-stress

profiles can be explained as a combination of distortion due to the vortices and of the 'stress-wave' or 'stress-bore' phenomenon described by Smits *et al.* in a boundary layer following a region of very strong streamline curvature. The bore arises only in flows where the curvature changes suddenly, resulting in a rapid increase (say) in Reynolds stresses in the fast-responding, moderate-size eddies near the outer edge of the inner layer, the increase then being convected into the outer layer by large-eddy eruptions. Again, however, the fact that a modest 'bore' also occurs in the dimensionless shear correlation coefficient implies real changes in turbulence structure as well as mere amplification. There is no evidence of a stress bore in $\overline{v^2}/\overline{u^2}$ (figure 10*d*), but the fact that this particular ratio increases suggests an increasing tendency to outward eruptions: interestingly, the corresponding decrease in $\overline{v^2}/\overline{u^2}$ in the convex case is barely significant.

The spanwise variations in shear correlation coefficient and stress/energy ratio, both of which are moderately independent of distance from the surface in a conventional boundary layer, may be due to the spanwise variation of $\partial V/\partial y$, which is positive when the flow between the two vortices is moving outwards and negative when the 'common' flow is moving inwards. It is well known from flow-visualization photographs, such as those of Head & Bandyopadhyay (1978), that accelerated boundary layers with positive $\partial U/\partial x$ and negative $\partial V/\partial y$ suffer severe 'flattening' of the eddies (strictly, of the boundaries of the smoke-filled flow), which is likely to lead to significant structural changes. In the present case, $\partial V/\partial y$ is balanced by $\partial W/\partial z$ rather than $\partial U/\partial x$, but some 'flattening' of eddies is to be expected: certainly, the shear-stress parameters are smaller at the 'crest' – i.e. the position of maximum negative $\partial V/\partial y$ – than at the 'trough'.

In contrast to the behaviour found by Smits *et al.*, the triple products in the present experiment do not exhibit a significant 'bore' behaviour. As shown in figure 11, the streamwise variation of the transport velocities of shear stress and of turbulent energy is smooth, suggesting a gentle amplification and/or tilting of the initial profile with increasing x. Smits *et al.* concluded from their measurements that transport equations for triple products, or transport velocities, would be needed in flows with rapidly changing curvature, but in mildly curved flows like the present one an algebraic relation between the transport velocity or eddy diffusivity and the shape of the shear-stress profile may be adequate. Certainly, the changes in shear-stress transport velocity in the outer layer are sufficiently small to present no very significant modelling problem, while in the inner layer the turbulent transport terms are small.

As mentioned above, the difference between turbulent-zone averages and conventional averages is best discussed in terms of the non-turbulent-zone averages, because the three are connected by (3). The shear correlation coefficient in the irrotational zone increases moderately with increasing x (i.e. increasing δ/R). Fractional increase in the irrotational-zone R_{uv} in the outermost part of the boundary layer are extremely large, and would be even larger if the results were scaled on some characteristic thickness of the intermittency distribution (figure 13) rather than on the boundary-layer thickness derived from the mean-velocity profile. However, in an intermittent region the present simple choice of the conventional average as a baseline from which to measure fluctuations is not necessarily physically meaningful: the most meaningful choice of baseline for (say) the turbulent region is probably the zone-average velocity in the *non*-turbulent region.

As shown in figure 18, the increase in dissipation-length parameter L due to destabilizing curvature is considerably larger at the 'crest' (maximum c_f, minimum δ, minimum shear stress in the outer layer) than at the 'trough'. Indeed, values of

L/δ in the outer part of the 'trough' boundary layer are less than in the plane-surface boundary layer. It would be unwise to attribute these differences entirely to the effect of $\partial V/\partial y$ discussed above, but there is no obvious alternative reason. Any lengthscale used instead of δ to non-dimensionalize the results would have to have a spanwise variation considerably larger than that of δ or of any scale of the intermittency distribution: the implication is that the structural changes are real, rather than the result of a simplistic or inappropriate choice of scaling length.

Curvature, of either sign, has little effect on the turbulent- and non-turbulent-burst lengths at a given value of intermittency. This is in surprising contrast to the large changes in the dissipation-length parameter in the present experiments and in the autocorrelation integral (time-)scale measured by Ramaprian & Shivaprasad. This is a useful simplification for those directly concerned with the role of interface statistics in turbulent mixing and combustion, but from the present viewpoint the conclusion is that, unfortunately, interface statistics may not be useful for exploring the large eddies.

At the outset of the work, it was hoped that there would be a useful interaction between it and the studies of artificially generated imbedded longitudinal vortex pairs on flat surfaces reported by Mehta & Bradshaw (1985) and Shibl & Bradshaw (1985). In the event, only rather gross correspondences can be found between vortex-pair flows and the infinite array of longitudinal vortices generated by destabilizing streamline curvature. Part of the reason is that vortex pairs with the 'common flow' between them in the upward direction tend to migrate out of the boundary layer, while vortices with the 'common flow' downwards repel each other in the spanwise direction; but the main difficulty in drawing parallels is that spanwise variations are not the only effect of streamline curvature.

5. Conclusions

This paper and the companion paper of Muck, Hoffmann & Bradshaw (1985) clearly demonstrate the implication of previous work, that the stabilizing and destabilizing effects of streamline curvature are essentially separate phenomena. Although stabilizing curvature produces significant changes in structural parameters such as the shear correlation coefficient, it is primarily the attenuation of an existing eddy structure. The interpretation of measurements with destabilizing (concave) curvature depends on how steady the longitudinal vortex structure is: in the present work, we deliberately fixed the vortex structure by introducing (small) disturbances far upstream, so that the primary effect of surface curvature on the turbulent structure could be distinguished from the secondary effects of the vortices. We have shown that, at least in the case of moderate curvature ($\delta/R = O(0.01)$), this primary effect is more important than the effect of the vortices: the practical conclusion is that calculation methods that represent the former, but take spanwise averages to eliminate the latter, may be quite satisfactory for engineering purposes. If the curvature is moderate, the percentage spanwise variation of surface shear stress and heat-transfer rate is sufficiently small that, for instance, spanwise variations of turbine-blade temperature could probably be neglected in estimations of creep life, remembering that in this particular case the ratio of boundary-layer thickness (and thus vortex wavelength) to blade thickness is likely to be fairly small.

The measurements do not indicate any simple way of allowing for curvature effects in calculation methods. It was clear from the results of the 1980–81 Stanford meeting (Kline *et al.* 1982) that turbulence models developed for plane flows do not naturally

produce the effect of curvature to acceptable accuracy, so that the main terms in model transport equations must contain coefficients depending explicitly upon (say) the ratio of turbulence lengthscale to streamline curvature. This is simply a special case of Kline's argument that an entirely general turbulence model (other than that provided by the nominally exact Navier–Stokes equations) is unlikely to be discovered in the future.

The work of P. H. Hoffmann was supported by the Brown, Boveri Research Center, and we are grateful to Dr M. P. Escudier for advice and encouragement.

REFERENCES

ANDREOPOULOS, J. & BRADSHAW, P. 1980 Measurements of interacting turbulent shear layers in the near wake of a flat plate. *J. Fluid Mech.* **100**, 639.

BARLOW, R. S. & JOHNSTON, J. P. 1985 Roll-cell structure in a concave turbulent boundary layer. *AIAA paper no.* 85-0297.

HEAD, M. R. & BANDYOPADHYAY, P. 1978 Combined flow visualization and hot wire measurements in turbulent boundary layers. In *Proc. AFOSR/Lehigh Workshop on Coherent Structure of Turbulent Boundary Layers* (ed. C. R. Smith & D. E. Abbott). Lehigh University.

HOFFMANN, P. H. & BRADSHAW, P. 1981 Turbulent boundary layers on concave surfaces. *Final Report to Brown Boveri Research Centre, Imperial College Aero TN* 81–111.

HUNT, I. A. & JOUBERT, P. N. 1979 Effects of small streamline curvature on turbulent duct flow. *J. Fluid Mech.* **91**, 633.

JEANS, A. H. & JOHNSTON, J. P. 1982 The effects of streamwise concave curvature on turbulent boundary layer structure. *Stanford Univ. Thermosci. Div. Rep. MD*-40.

JOHNSTON, J. P., HALLEEN, R. M. & LEZIUS, D. K. 1972 Effects of spanwise rotation on the structure of two-dimensional fully developed channel flow. *J. Fluid Mech.* **56**, 533.

KLINE, S. J., CANTWELL, B. J. & LILLEY, G. M. (eds) 1982 In *Proc. 1980–81 AFOSR-HTTM-Stanford Conference on Computation of Complex Turbulent Flows*, Thermosciences Divn., Stanford University.

MEHTA, R. D. & BRADSHAW, P. 1985 Longitudinal vortices imbedded in turbulent boundary layers. Part 2. Vortex pair with 'common flow' away from the surface. Submitted to *J. Fluid Mech.*

MERONEY, R. N. & BRADSHAW, P. 1975 Turbulent boundary layer growth over a longitudinally curved surface. *AIAA J.* **13**, 1448.

MOSER, R. D. & MOIN, P. 1984 Direct numerical simulation of curved turbulent channel flow. *NASA TM* 85974.

MUCK, K. C. 1982 Turbulent boundary layers on mildly curved surfaces. Ph.D. thesis, Imperial College, London.

MUCK, K. C., HOFFMANN, P. H. & BRADSHAW, P. 1985 The effect of convex surface curvature on turbulent boundary layers. *J. Fluid Mech.* **161**, 347–369.

PATEL, V. C. 1965 Calibration of the Preston tube and limitations on its use in pressure gradients. *J. Fluid Mech.* **23**, 185.

RAMAPRIAN, B. R. & SHIVAPRASAD, B. G. 1978 The structure of turbulent boundary layers along mildly curved surfaces. *J. Fluid Mech.* **85**, 273.

SHIBL, A. & BRADSHAW, P. 1985 Longitudinal vortices imbedded in turbulent boundary layers. Part 3. Vortex pair with 'common flow' towards the surface. To be submitted to *J. Fluid Mech.*

SMITS, A. J., YOUNG, S. T. B. & BRADSHAW, P. 1979 The effect of short regions of high surface curvature on turbulent boundary layers. *J. Fluid Mech.* **94**, 209.

SO, R. M. C. & MELLOR, G. L. 1975 Experiments on turbulent boundary layers on a concave wall. *Aero. Quart.* **26**, 35.

TANI, I. 1962 Production of longitudinal vortices in the boundary layer along a concave wall. *J. Geophys. Res.* **67**, 3075.

WATMUFF, J. H., WITT, H. T. & JOUBERT, P. N. 1985 Developing boundary layers with system rotation. *J. Fluid Mech.* **157**, 405.